Mapping the effects of physical and chemical reduction parameters on local atomic distributions within bimetallic nanoparticles

Hannah M. Johnson,[a] Acacia M. Dasher,[a] Madison Monahan,[b] Soenke Seifert,[c] and Liane M. Moreau*[a]

[a] Department of Chemistry, Washington State University, Pullman, WA 99164, USA
[b] Department of Chemistry, University of Washington, Seattle, WA 98195, USA
[c] X-ray Sciences Division, Argonne National Laboratory, Argonne, IL 60439, USA

Supporting Information

UV-Vis Absorbance Spectra

Figure S1: Absorbance spectra of AgAu NPs synthesized with a 1:1 ratio of metal:reductant using the v1 (concentrated) volume method.

Figure S2: Absorbance spectra of AgAu NPs synthesized with a 1:2 ratio of metal:reductant using the v1 (concentrated) volume method.
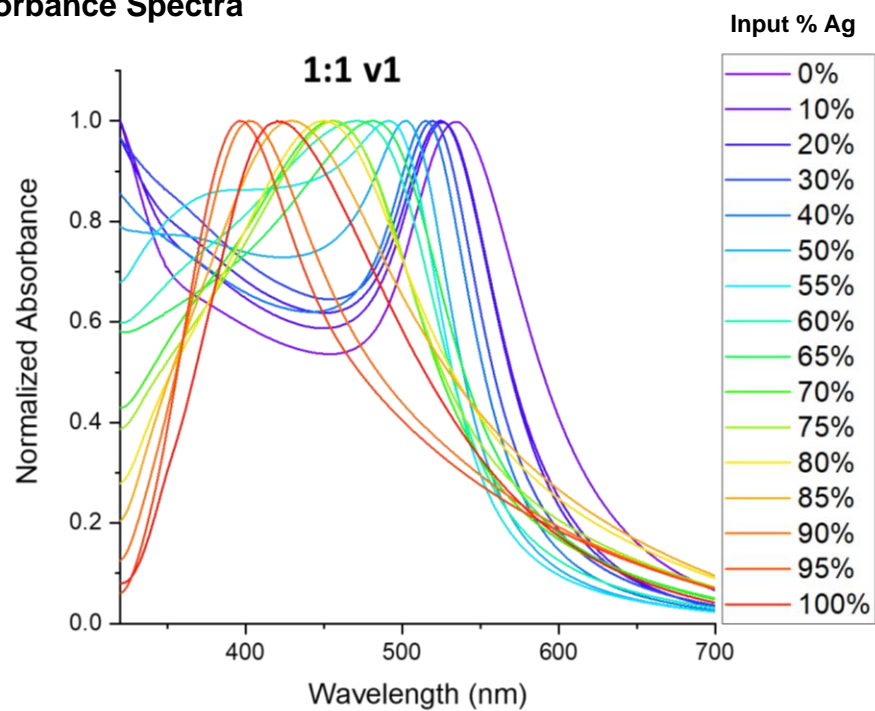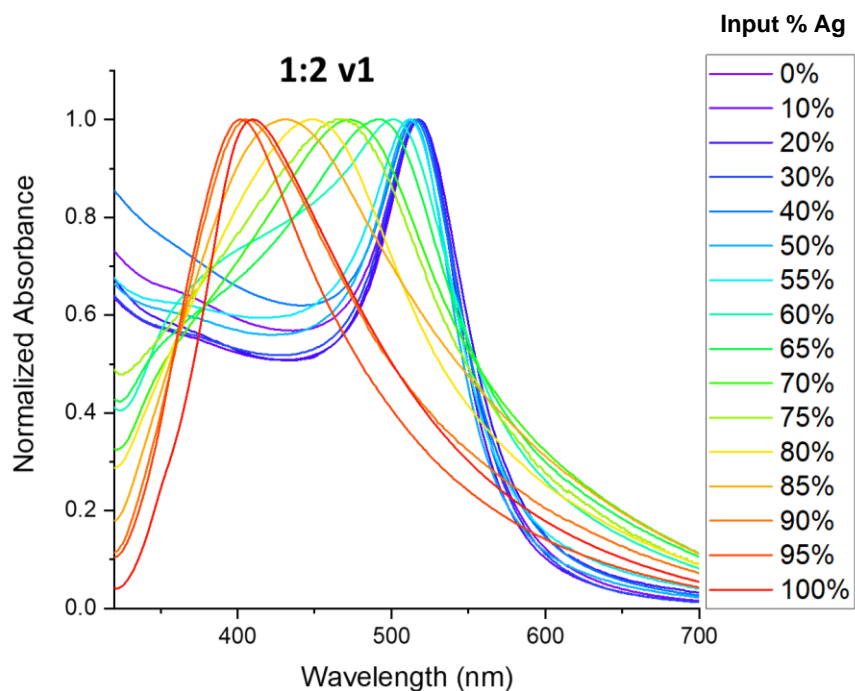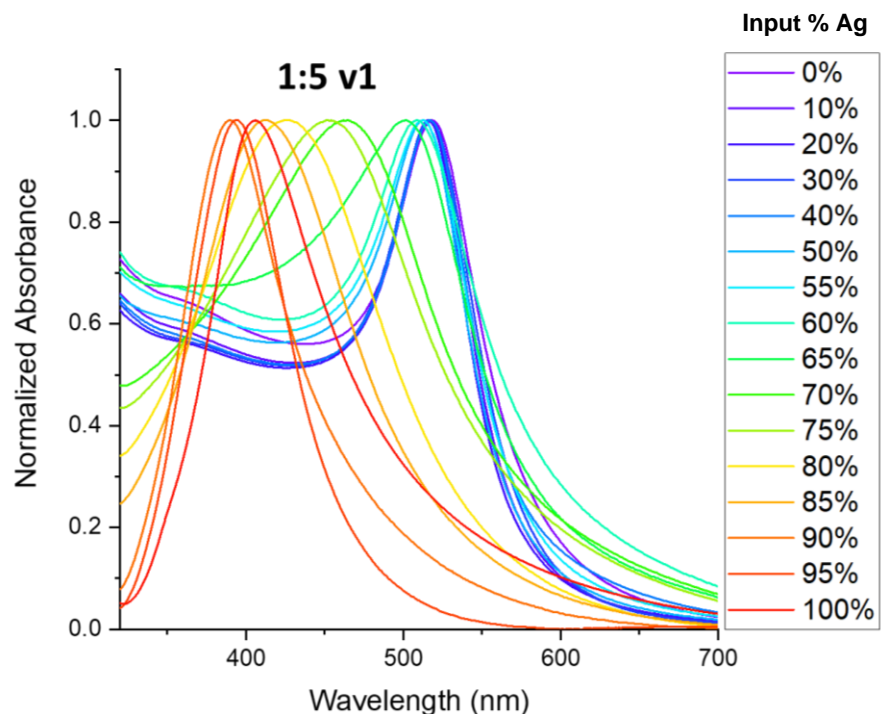
Figure S3: Absorbance spectra of AgAu NPs synthesized with a 1:5 ratio of metal:reductant using the v1 (concentrated) volume method.

Figure S4: Absorbance spectra of AgAu NPs synthesized with a 1:5 ratio of metal:reductant using the v2 (dilute) volume method.

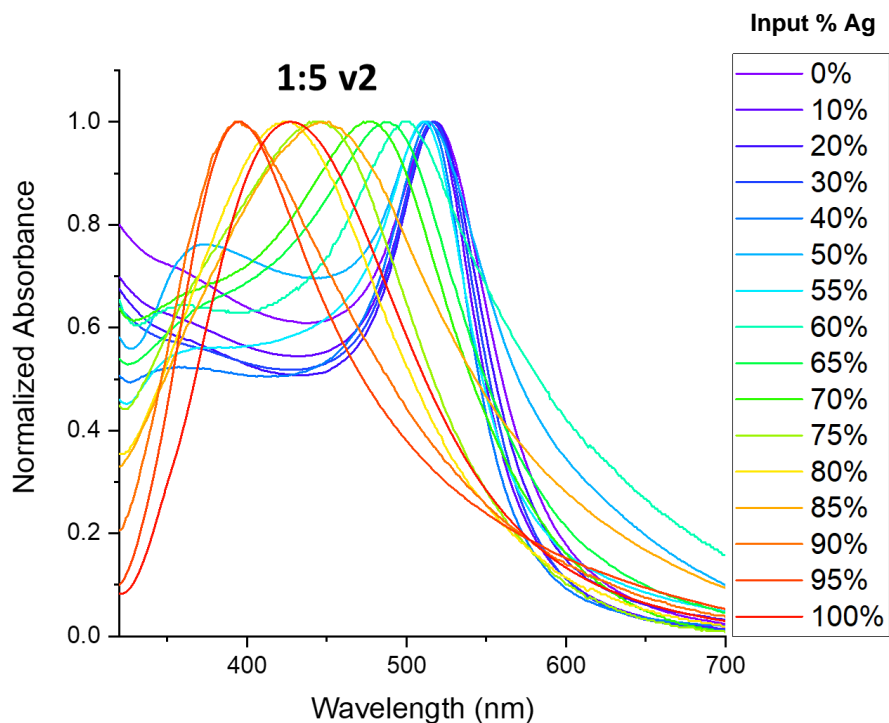**Figure S5:** Absorbance spectra of AgAu NPs synthesized with a 1:10 ratio of metal:reductant using the v1 (concentrated) volume method. The shoulder feature at ~350 nm is higher in intensity than the LSPR peak itself, skewing normalization, but the peak shift resembles that of other methods.
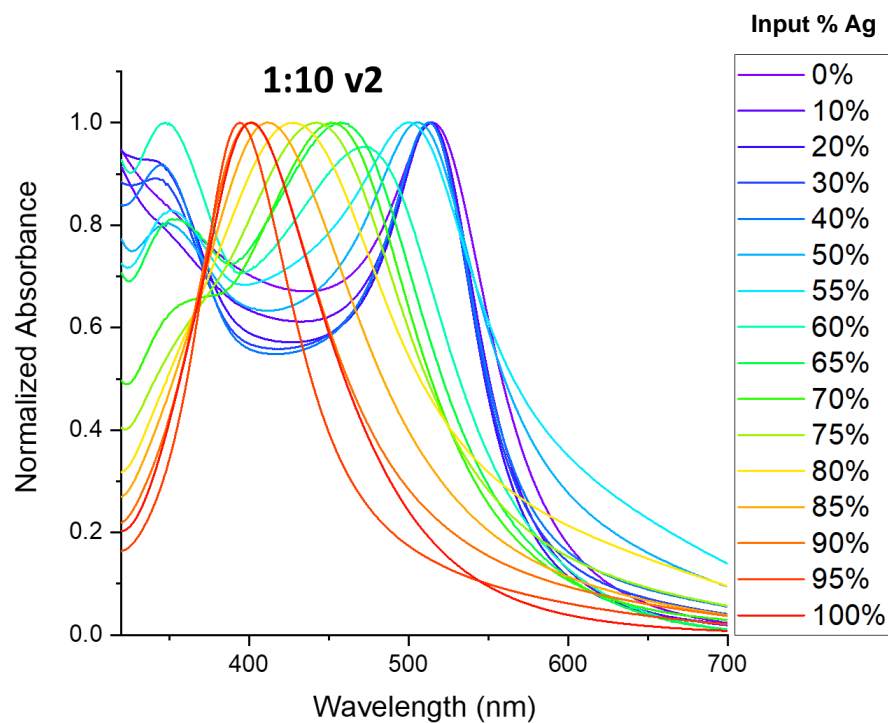
Figure S6: Absorbance spectra of AgAu NPs synthesized with a 1:10 ratio of metal:reductant using the v2 (dilute) volume method.
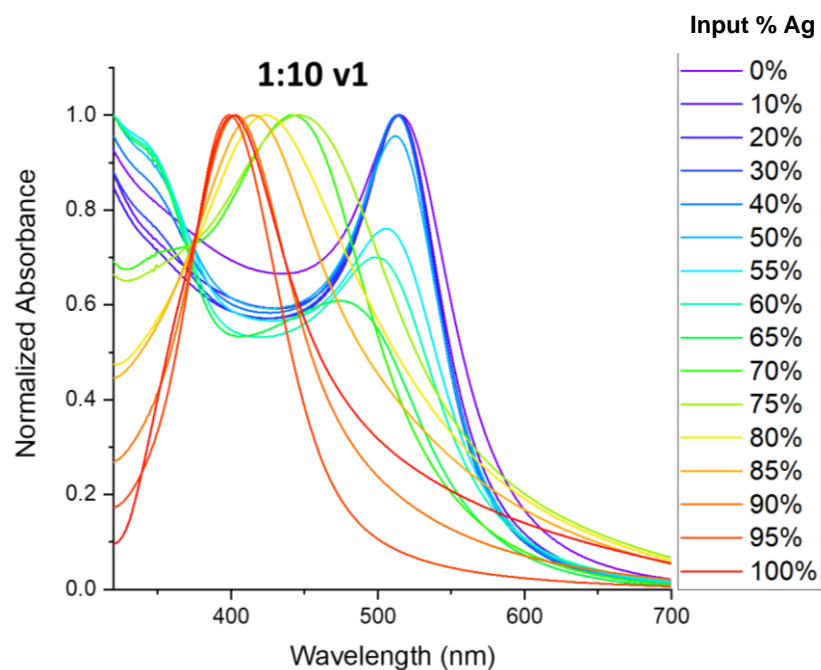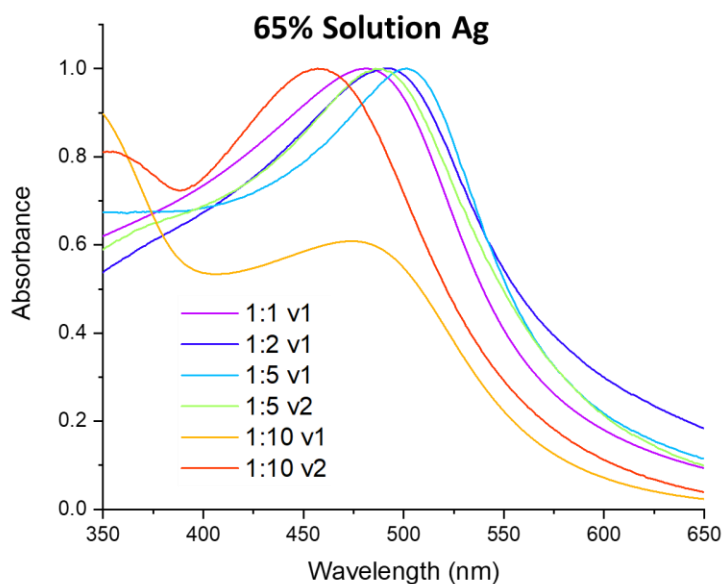
Figure S7: Absorbance spectra of AgAu NPs synthesized with a starting metal solution composed of 65% Ag (determined by XRF to actually represent a 28 ± 3% Ag NP). The optical signature obtained varies drastically depending on the reducing condition employed, which cannot be explained by size, shape, or composition effects alone; this instead suggests differences in the distribution and homogeneity of the alloy.

X-Ray Fluorescence

Figure S8: A representative XRF spectrum of the AgAu NPs with Au and Ag lines labeled; only Au L$_\alpha$ and Ag K$_\alpha$ were used to quantify composition. Lines marked with * are Zr K$_\alpha$ and K$_\beta$ lines resulting from internal instrumental components.
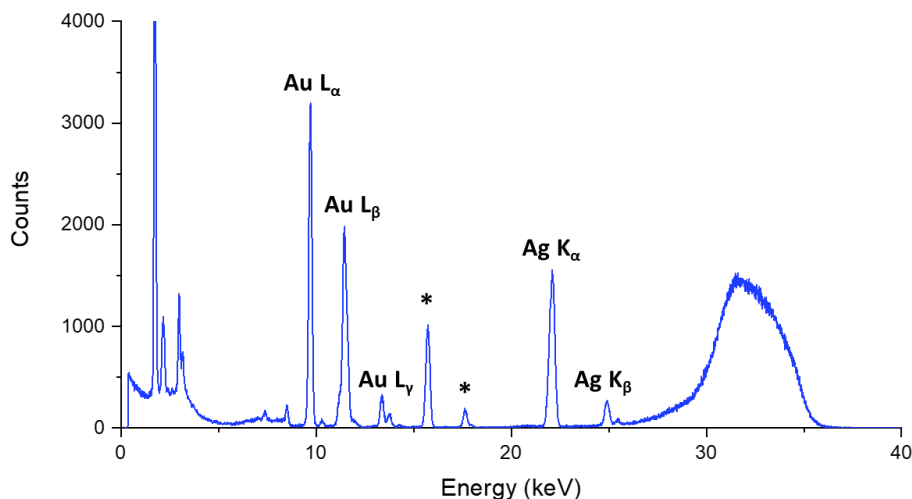
Table S1: The relative percent composition of silver (% Ag) in each NP sample as calculated by the Bruker S4 T-Star ESPRIT software. The error associated with each measurement was below ± 0.3% and is not individually reported.

Solution % Ag	Actual % Ag in NP					Average NP % Ag
	1:1 v1	1:5 v1	1:5 v2	1:10 v1	1:10 v2	
10%	2.428	2.607	4.230	3.213	4.011	4.0 ± 0.7
20%	2.067	4.464	6.550	5.565	7.212	5 ± 2
30%	2.829	6.454	8.971	7.024	9.068	7 ± 2
40%	4.817	8.009	12.00	8.013	14.20	9 ± 3
50%	9.343	8.327	15.06	11.05	13.56	12 ± 2
55%	8.979	18.00	21.60	6.735	18.28	15 ± 6
60%	18.88	17.95	21.47	24.03	18.20	20 ± 2
65%	27.62	21.48	31.12	30.92	29.38	28 ± 3
70%	27.82	36.03	36.34	40.21	33.29	34 ± 4
75%	44.48	39.66	43.67	48.19	46.02	44 ± 3
80%	51.83	49.42	52.70	56.62	51.65	52 ± 2
85%	63.06	59.32	67.19	65.81	66.07	64 ± 3
90%	71.91	75.64	73.60	73.91	75.48	74 ± 1
95%	82.42	86.74	89.03	89.37	89.73	87 ± 3

Small Angle X-Ray Scattering

Extended Methods

Raw CCD images containing 2D scattering patterns were reduced to 1D q-space patterns in NIKA[1]. The sample-to-detector distance was refined using the pattern of a silver behenate calibrant, the beamstop was manually masked, and 20 scans per sample were reduced and averaged to yield the sample pattern used in fitting. This was also performed for several blank water scans taken periodically throughout the data collection period.

Each averaged sample was background subtracted in IRENA[2] with the blank water scan collected closest in time to the sample, in order to account for any systematic drift in beam flux. Background-subtracted patterns were fit for particle size and polydispersity to a spheroid form factor over a Schulz-Zimm distribution, assuming a dilute structure factor of 1 due to the nanomolar concentrations of particles used. The fit was generally performed from q = 0.02–0.08 Å^{-1} (± 0.01 Å^{-1}), encapsulating the morphologically descriptive scattering features while avoiding the noise of high q from background subtraction and the complications resulting from particle aggregation at low q (Guinier region). Four parameters were allowed to vary to achieve minimization of χ^2: size, polydispersity, a flat (fixed-value) background independent of the subtracted water blank, and a scaling factor.
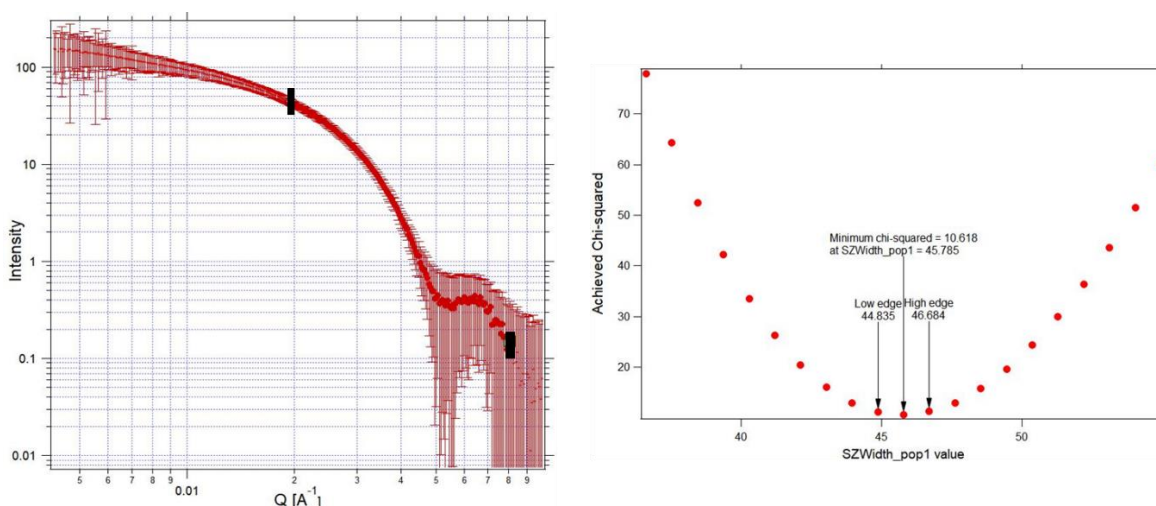
Figure S9: A representative SAXS pattern of the AgAu NPs; marked in black is fitting region. Fit optimization determines the optimal values of size and polydispersity to minimize χ^2.

Tables S2 – S7: The results of each fit are displayed in the following tables, including the calculated particle diameter in nm and its error, the size width (*i.e.* polydispersity) in nm and its error, and the adjusted chi-square associated with the fit. The samples marked with † were not sufficiently stable to be cleaned and concentrated for SAXS; these sizes were estimated via TEM instead (see Fig. S9).

Table S2: 1:1 v1					
Input % Ag	Size (d, nm)	Error (± nm)	Width (nm)	Error (± nm)	Adjusted χ^2
0% †	50	---	10	---	---
10%	22.258	0.009	6.6	0.2	17.1
20%	17.80	0.04	5.3	0.2	18.1
30%	15.10	0.03	4.9	0.3	4.09
40%	15.501	0.005	4.3	0.1	18.2
50%	14.70	0.01	7.77	0.05	8.57
55%	19.294	0.008	11.95	0.09	13.5
60%	16.495	0.003	6.74	0.04	16.3
65%	20.376	0.006	16.43	0.04	7.75
70%	17.849	0.008	11.26	0.08	22.4
75%	17.23	0.03	9.0	0.2	24.0
80%	19.015	0.006	12.46	0.05	10.7
85%	19.302	0.007	12.17	0.07	13.4
90%	19.842	0.007	9.6	0.1	12.9
95%	19.77	0.05	10.0	0.3	22.6
100% †	110	---	25	---	---

Table S3: 1:2 v1					
Input % Ag	Size (d, nm)	Error (± nm)	Width (nm)	Error (± nm)	Adjusted χ^2
0%	27.4	0.3	15.2	0.4	18.7
10%	15.945	0.002	5.54	0.02	24.1
20%	16.443	0.001	6.36	0.01	13.2
30%	16.960	0.002	6.69	0.02	17.4
40%	17.023	0.001	7.19	0.01	9.70
50%	17.408	0.002	7.40	0.02	11.1
55%	17.418	0.007	7.64	0.05	24.8
60%	15.65	0.03	7.3	0.1	16.9
65%	15.29	0.05	7.3	0.2	17.8
70%	16.3	0.2	10.0	0.2	22.7
75%	17.2	0.1	11.8	0.3	20.5
80%	17.4	0.1	12.2	0.2	24.9
85%	18.1	0.2	14.2	0.3	3.75
90%	18.961	0.008	13.55	0.08	10.5
95%	22.68	0.02	9.1	0.2	10.6
100% †	70	---	15	---	---

	Table S4: 1:5 v1				
Input % Ag	Size (d, nm)	Error (± nm)	Width (nm)	Error (± nm)	Adjusted χ^2
0%	14.836	0.006	5.80	0.05	27.7
10%	15.022	0.008	6.51	0.04	24.6
20%	15.976	0.004	6.61	0.03	22.9
30%	16.354	0.004	7.02	0.04	20.4
40%	15.924	0.003	6.80	0.03	20.0
50%	15.72	0.01	6.94	0.06	22.6
55%	16.024	0.008	6.76	0.05	24.4
60%	14.722	0.008	5.56	0.06	22.5
65%	14.42	0.03	6.2	0.1	44.2
70%	13.40	0.06	7.1	0.2	15.3
75%	13.0	0.2	7.3	0.2	18.5
80%	14.30	0.08	9.0	0.3	22.4
85%	16.6	0.2	14.6	0.6	19.7
90%	18.84	0.03	15.4	0.2	9.17
95%	22.374	0.006	12.50	0.06	7.42
100%	42.3	0.8	18	2	28.6

	Table S5: 1:5 v2				
Input % Ag	Size (d, nm)	Error (± nm)	Width (nm)	Error (± nm)	Adjusted χ^2
0%	15.682	0.004	4.78	0.06	21.4
10%	14.288	0.001	4.49	0.01	15.3
20%	14.3646	0.0007	4.230	0.008	14.4
30%	14.204	0.002	4.24	0.02	17.2
40%	14.558	0.001	4.24	0.02	18.1
50%	15.986	0.005	5.24	0.07	18.5
55%	15.61	0.04	8.0	0.2	29.3
60%	14.25	0.03	7.9	0.2	23.5
65%	13.9	0.1	8.0	0.2	6.91
70%	13.2	0.1	7.3	0.2	1.42
75%	15.20	0.02	9.2	0.2	22.9
80%	15.30	0.02	9.5	0.2	19.1
85%	15.59	0.02	9.9	0.2	18.3
90%	17.44	0.01	9.5	0.1	11.6
95%	21.02	0.02	10.3	0.2	11.2
100%	42	1	31	4	21.2

	Table S6: 1:10 v1				
Input % Ag	**Size (d, nm)**	**Error (± nm)**	**Width (nm)**	**Error (± nm)**	**Adjusted χ^2**
0%	14.62	0.03	7.4	0.1	23.1
10%	14.226	0.005	5.88	0.04	21.4
20%	14.470	0.003	5.74	0.04	24.7
30%	15.230	0.004	6.32	0.03	20.5
40%	15.2732	0.0008	6.19	0.02	5.46
50%	15.764	0.001	6.30	0.02	9.81
55%	15.303	0.009	6.66	0.08	19.6
60%	13.944	0.006	4.92	0.07	16.1
65%	13.38	0.02	5.8	0.1	26.6
70%	12.64	0.02	5.9	0.1	9.50
75%	15.514	0.003	4.48	0.09	15.8
80%	13.28	0.03	7.5	0.2	16.1
85%	16.16	0.04	10.6	0.2	25.2
90%	14.228	0.002	4.258	0.002	25.1
95%	21.5	0.1	13.1	0.3	29.4
100%	50	3	39	5	8.59

|	Table S7: 1:10 v2				
Input % Ag	**Size (d, nm)**	**Error (± nm)**	**Width (nm)**	**Error (± nm)**	**Adjusted χ^2**
0%	12.6	0.1	4.94	0.08	13.1
10%	12.840	0.008	4.08	0.03	11.6
20%	12.734	0.001	3.44	0.02	17.5
30%	12.846	0.002	3.38	0.04	22.5
40%	13.246	0.002	3.54	0.05	24.0
50%	13.728	0.003	4.22	0.06	10.2
55%	13.607	0.008	5.4	0.1	10.2
60%	12.92	0.02	4.9	0.1	9.31
65%	12.08	0.07	6.2	0.2	18.0
70%	13.14	0.01	6.3	0.1	15.6
75%	11.42	0.04	5.8	0.1	7.29
80%	13.538	0.007	7.3	0.1	5.44
85%	16.60	0.01	12.7	0.1	7.02
90%	15.530	0.009	8.4	0.1	7.51
95%	20.49	0.06	12.7	0.2	14.2
100%	69	2	32	6	26.5

TEM Images
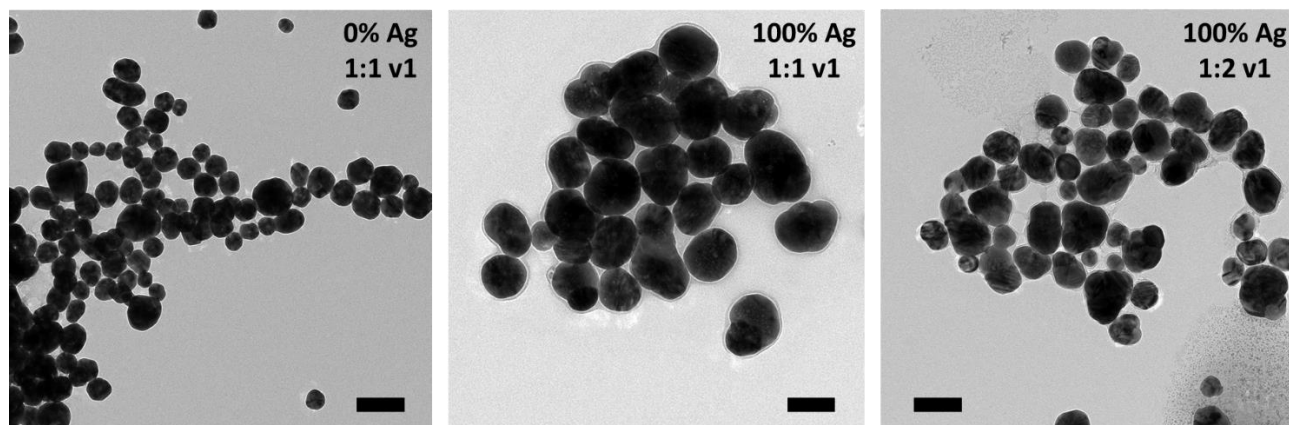
Figure S10: TEM images of the three samples that were not analyzed by SAXS (marked with † in Table S2 and S3); the low reductant ratios resulted in large, weakly-capped particles that could not withstand repeated centrifugation and washing. Scale bar = 100 nm.
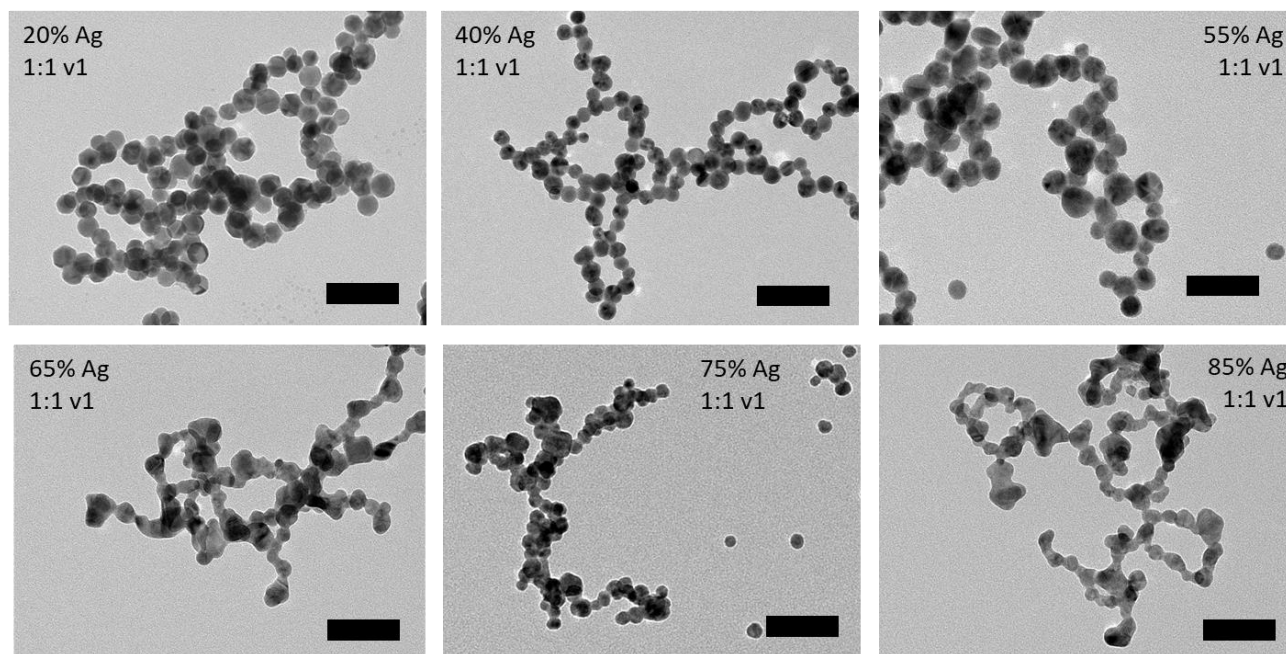

Figure S11: Additional representative TEM images of bimetallic AgAu NPs of various compositions. The % Ag label in each picture refers to the reaction solution composition, not that of the resulting particle. The gradual increase in propensity to fuse is apparent as the particles become more silver-rich, particularly at their surfaces. This demonstrates the need to pursue other statistical determinations of size and morphology, such as SAXS. Scale bar = 100 nm.

No grid treatment

With grid treatment
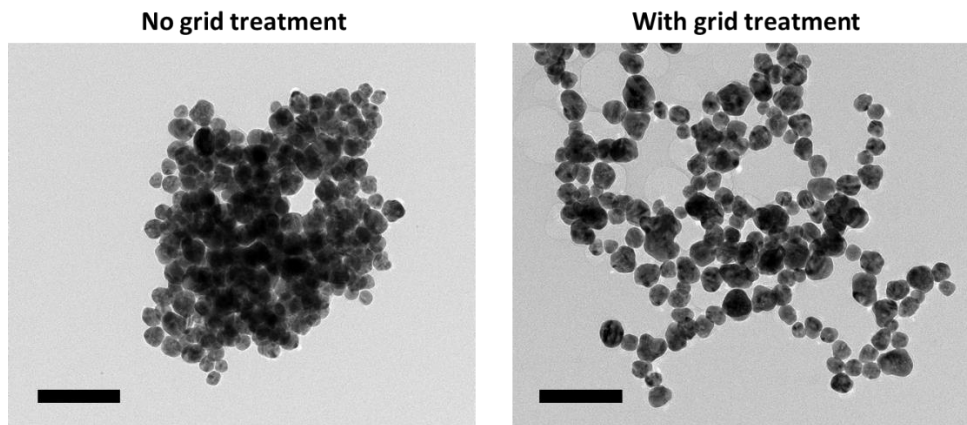
Figure S12: Pre-treatment of the TEM grid with 0.5 mM AA significantly aided the dispersion of particles on the grid and somewhat reduced fusing, as seen here with a sample of pure Ag NPs. Scale bar = 100 nm.
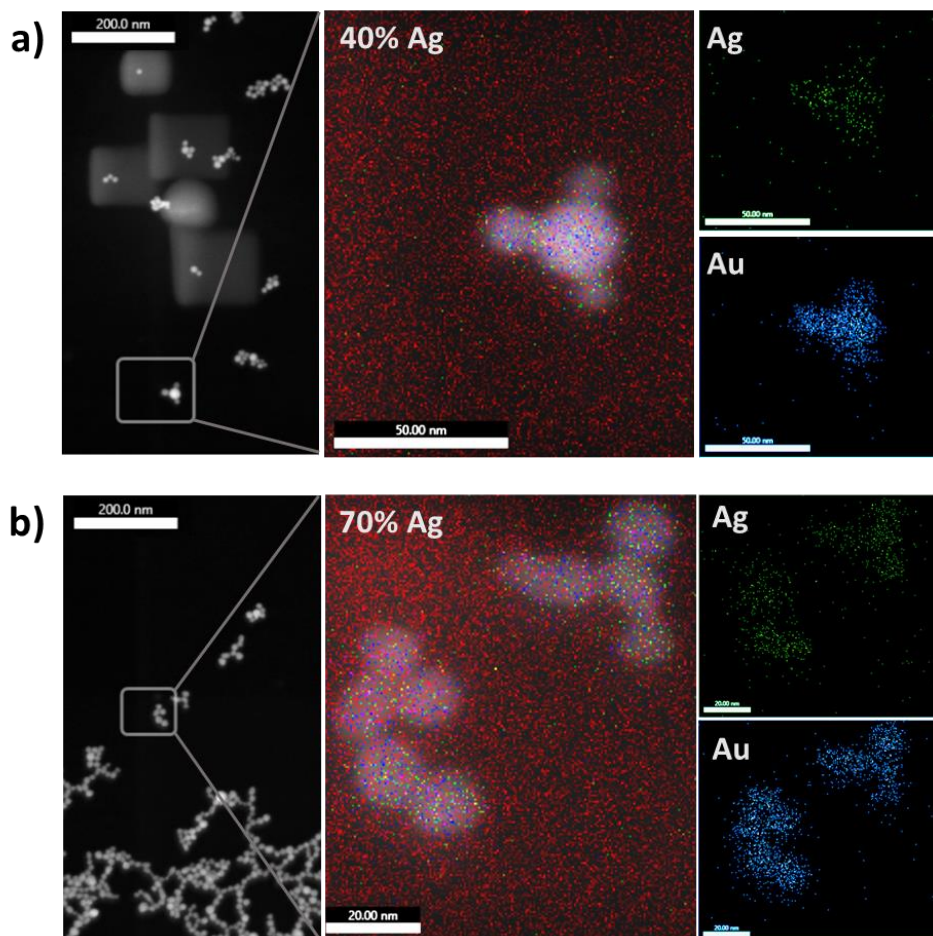
EDX Mapping

Figure S13: EDX maps of AgAuNPs made with a starting solution metal ratio of a) 40% Ag, and b) 70% Ag, corresponding to particles with an actual composition of 9 ± 3% and 34 ± 4% Ag, respectively. Despite limitations of low resolution, in neither case is a bimodal population of Au and Ag NPs observed, and in fact Au does appear to be concentrated more heavily in the particle centers while Ag appears to reside more diffusely on particle surfaces and edges.
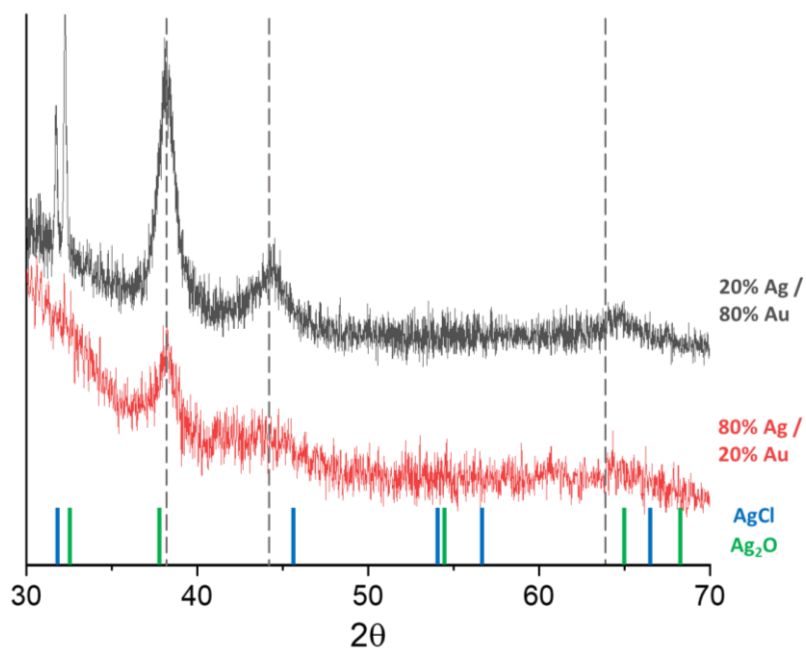
X-ray Diffraction

Figure S14: XRD patterns of dried AgAuNPs of different compositions. The dashed lines correspond to the expected peaks arising from bulk FCC metal, *i.e.* pure Au and Ag. The Scherrer broadening associated with nanoscale crystallite domains is apparent. Additional sharp diffraction peaks are seen from 30-35° in the case of 20% solution Ag that correspond to trace AgCl and/or Ag_2O, confirming the observations from EXAFS for this sample.

XAFS extended methods

Samples were selected for XAFS measurements to develop a representative set, where both the Ag:Au ratio space was explored, but also samples were collected at the same Ag:Au ratio with differing reductant ratios and volumes, in order to thoroughly survey all relevant parameters and their specific effects on the atomic scale Ag and Au distributions.

Based on this consideration, the following samples were measured: Au and Ag foil standards, 100% Au and 100% Ag NPs, and AgAu NPs including 20% Ag 1:1 v1, 20% Ag 1:5 v2, 50% Ag 1:1 v1, 50% Ag 1:10 v1, 50% Ag 1:10 v2, 50% Ag 1:5 v2, 65% Ag 1:10 v1, 65% Ag 1:1 v1, 85% Ag 1:10 v1 and 85% Ag 1:1 v1. It should be noted that all indicated percentages when reporting the XAFS spectra and associated parameters represent the % Ag precursor added rather than the % Ag actually incorporated into the NPs.

Absorption edge energy was determined from the maximum of the first derivative in the absorption data and the background was subtracted using the AUTOBK algorithm.[3] Data were processed and normalized to unity using a k-weight of 3 and an R_{bkg} parameter of 1.5. Multiple scans were merged in the case of transmission, or summed in the case of fluorescence, to improve statistics. Transmission data was used whenever possible, however low Ag incorporation % samples in particular at the Ag K edge required use of fluorescence spectra to improve fitting statistics. In all cases where fluorescence data was used, spectra were compared to data collected in transmission to ensure that self-absorption effects were not observed.

XANES spectra

Below, XANES spectra have been plotted at the Au L_3 and Ag K absorption edges. For better visualization, samples have been plotted comparing samples of a fixed atomic % Ag added to solution along with the pure metal case.
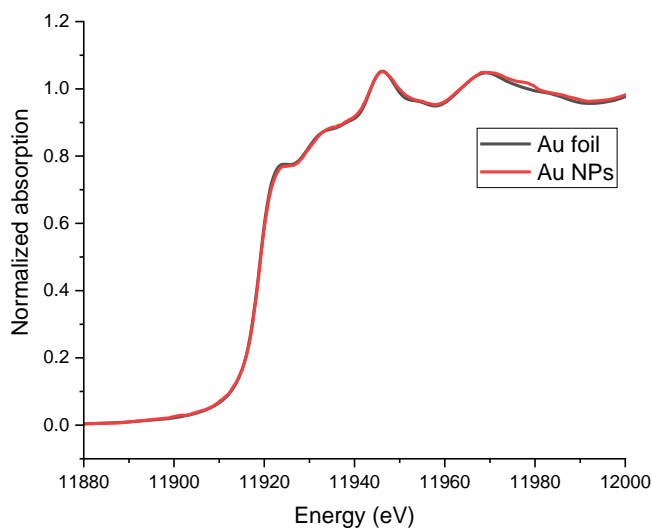

Figure S15.1 XANES data at the Au L_3 edge for an Au foil compared with 100% Au NPs shows that the NPs display the characteristic bulk spectrum.
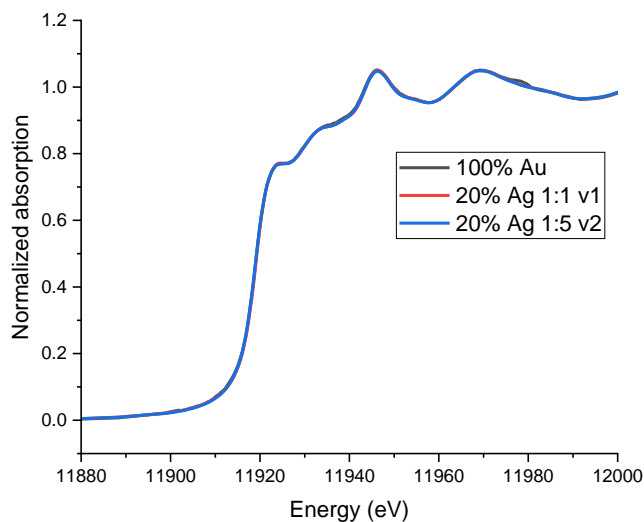

Figure S15.2 XANES data at the Au L_3 edge for 100% Au NPs compared with 20% Ag NPs shows that in both the 1:1 v1 case and 1:5 v2 case, the spectrum appears identical to pure Au.
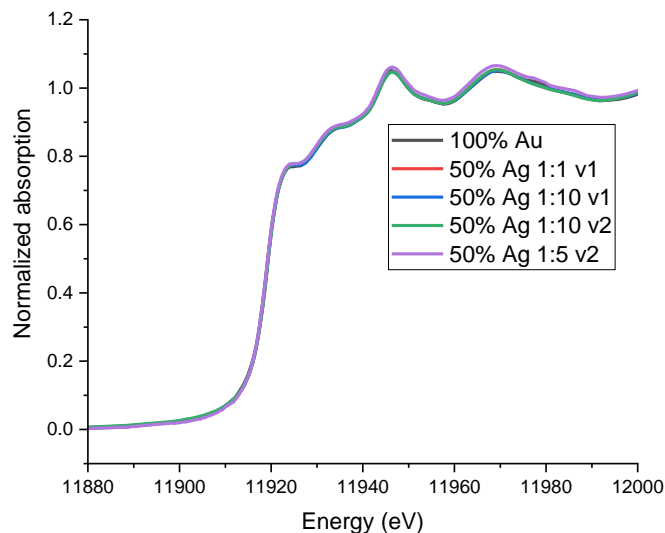
Figure S15.3 XANES data at the Au L₃ edge for 100% Au NPs compared with 50% Ag NPs exhibit the same characteristic spectra in all cases.
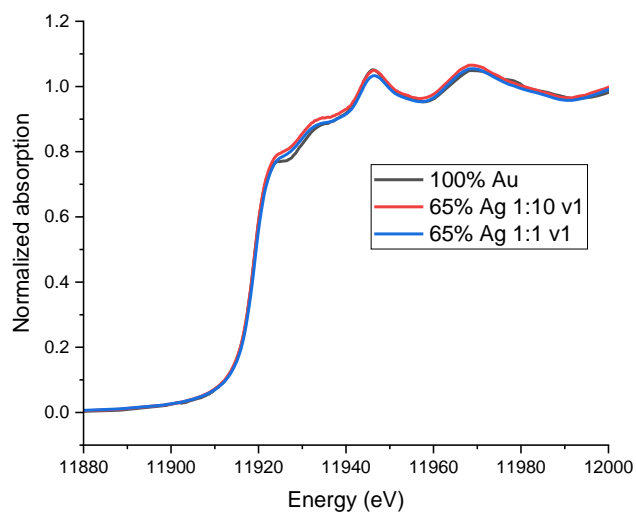

Figure S15.4 XANES data at the Au L₃ edge for 100% Au NPs compared with 65% Ag NPs shows that the Ag-containing spectra begin to deviate from bulk Au, with a dampened and increased region around the white line.
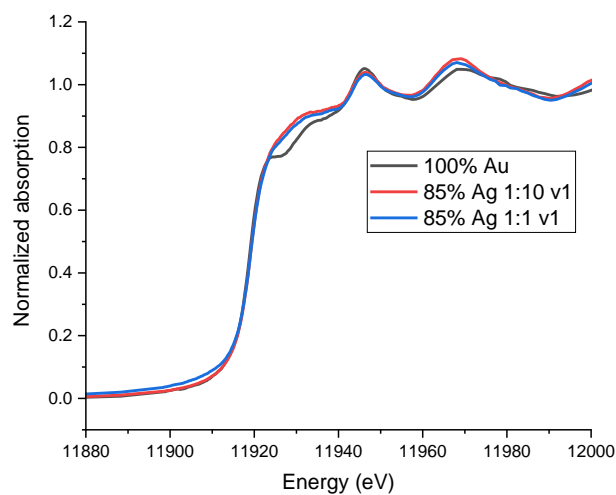
Figure S15.5 XANES data at the Au L_3 edge for 100% Au NPs compared with 85% Ag NPs shows that the Ag-containing spectra deviate considerably through dampening and rounding above the white line. This feature is indicative of a potential change despite retaining the Au^0 state.
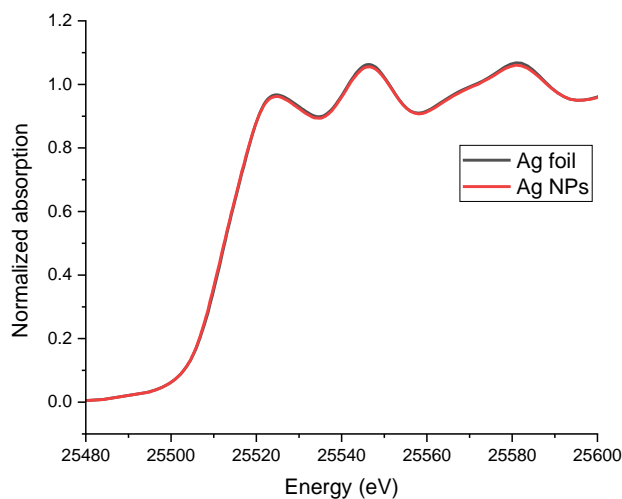

Figure S15.6 XANES data at the Ag K edge for an Ag foil compared with 100% Ag NPs shows that the NPs display the characteristic bulk spectrum.
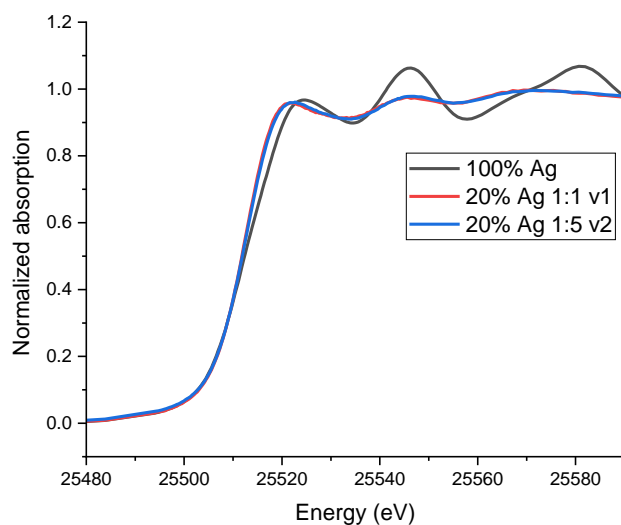
Figure S15.7 XANES data at the Ag K edge for 100% Ag NPs compared with the NPs where 20% of the solution precursor was Ag shows that in the 20% cases, the Ag exhibits Ag$^+$ characteristics, through a sharpening of the white line and different near edge features that more closely resemble AgCl[4] than Ag bulk.
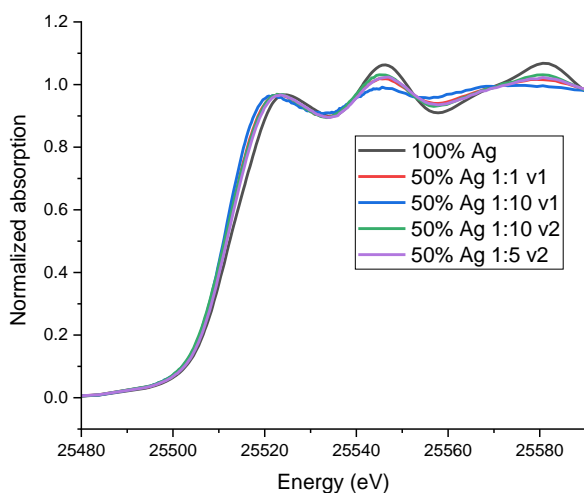

Figure S15.8 XANES data at the Ag K edge for 100% Ag NPs compared with the NPs where 50% of the solution precursor was Ag shows that the 50% 1:10 v1 sample exhibits similarities to the 20% samples shown in SX.7. The other samples all exhibit some deviation from the 100% Ag case, suggestive of potential changes from AgAu mixing.
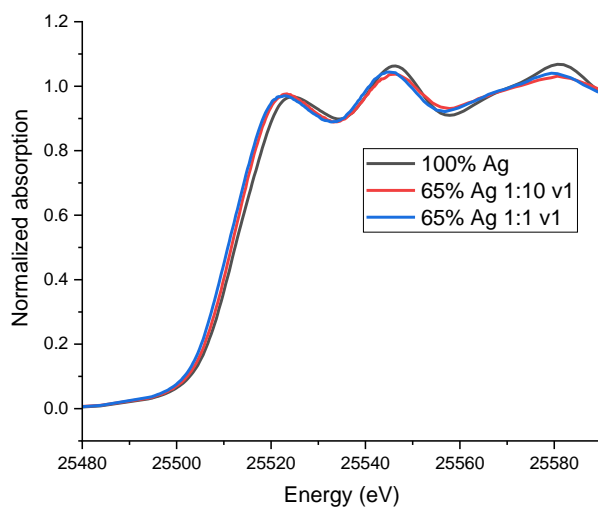
Figure S15.9 XANES data at the Ag K edge for 100% Ag NPs compared with the NPs where 65% of the solution precursor was Ag shows some deviation due to AgAu mixing, however the 65% signatures more closely resemble pure Ag.
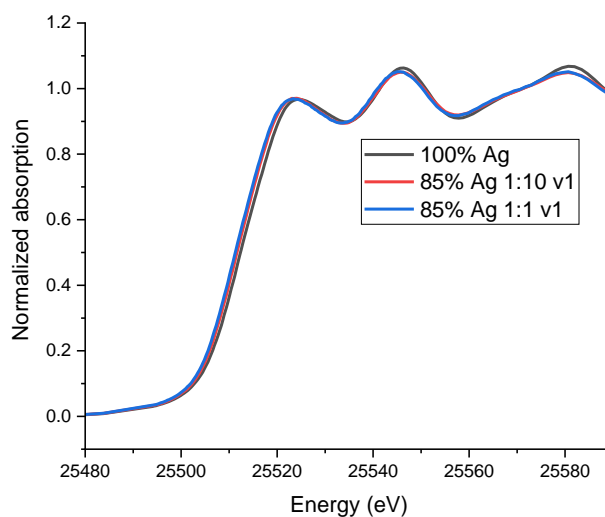

Figure. S15.10 XANES data at the Ag K edge for 100% Ag NPs compared with the NPs where 85% of the solution precursor was Ag shows minimal deviation due to AgAu mixing; the signatures are very similar to the pure Ag case.

EXAFS analysis extended methods

ARTEMIS, part of the IFEFFIT package software,[5] was used to reduce and fit the data to theoretically-generated pathways. Theoretical crystal structures for FCC Ag and Au and created structures where alternatively substituted as a second site with equivalent first-shell bondlengths were imported and converted to scattering pathways using ATOMS.[6] EXAFS spectra were modeled according to the EXAFS equation, a simplified version of which is:[7, 8, 9, 10]

$$\chi(k) = \sum_{\Gamma}\left[\frac{N_{\Gamma}S_0^2 F_{\Gamma}(k)}{2kR_{\Gamma}^2}e^{-2k^2\sigma_{\Gamma}^2}e^{-2R_{\Gamma}/\lambda(k)} \times \sin\left(2kR_{\Gamma} + \phi_{\Gamma}(k)\right)\right] \qquad (S1)$$

Where Γ is the summation over the individual scattering pathways, k is the photoelectron wavevector, $F_{\Gamma}(k)$ is the scattering amplitude, $\lambda(k)$ is the mean free path of inelastically-scattered photoelectrons and $\Phi(k)$ is the phase shift, which is calculated as a function of the absorbing and scattering atom. S_0^2, the amplitude reduction factor, was determined by fitting a bulk Ag or Au foil, and then applied to fitting all NP samples to more accurately extract the coordination numbers.[9] Degeneracy (N_{Γ}), half-path length (R_{Γ}), energy shift and mean-squared disorder (σ_{Γ}^2) were allowed to float in the fit for each included pathway in order to arrive at the best fit model. ΔE_0 was also allowed to float, but the same variable was used for all pathways. In certain cases, particularly for structures where the secondary bonding contribution was very low, σ_{Γ}^2 values were paired for both Au-Au and Au-Ag pathways to avoid a negative, unphysical value for this variable, which led to reasonable results.

Error bars for individual parameters were determined during the fitting process, taking into account the correlation matrix between variables. Reported error bars are estimated to one sigma (~ 68% confidence level). Spectra were fit in R-space using multiple k-weight fitting to arrive at the best fit model irrespective of chosen k-weight. Fitting in k-space and q-space yielded similar results, and were used to confirm the validity of the R-space fits, which are ultimately the reported results as shown in figure SX. Parameters reported without error bars were fixed during the fit.
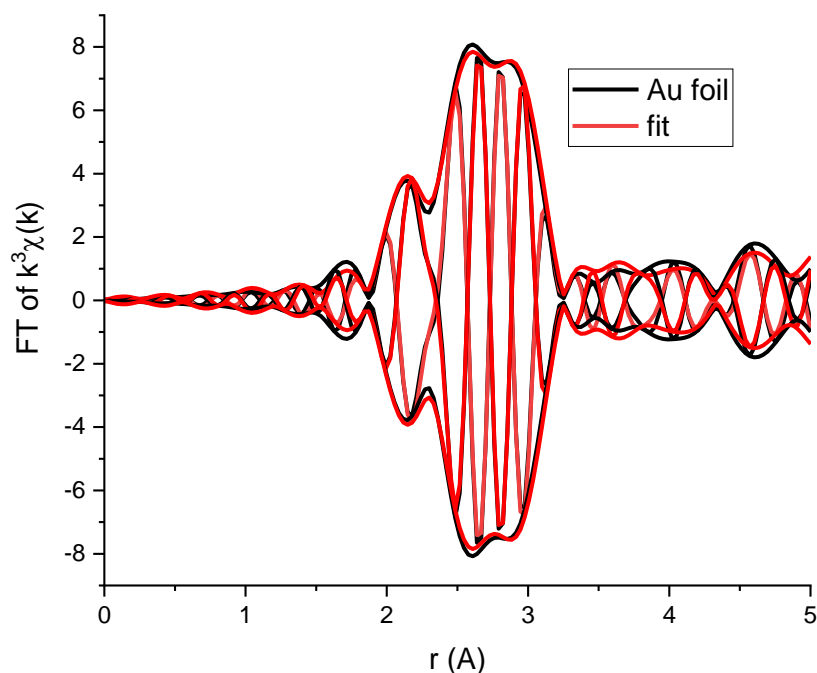
Sample	Path	N	R (Å)	σ^2 (Å^2)	ΔE_0 (eV)
Au foil (standard)	Au-Au	12	2.862(2)	0.0083(3)	4.9(2)
	Au-Au	6	4.05(14)	0.013(2)	
	Au-Au	24	4.986(8)	0.0123(8)	
	Au-Au	12	5.77(3)	0.009(3)	
	Au sink	ΔR (Å) = -0.015(1)		0.011(2)	
$S_0^2 =$ 0.85(4)				**R-factor** = 0.009	

Figure S16.1 Fit results from bulk Au foil. A bulk foil was fit to extract the S_0^2 parameter and to consider reasonability of NP-extracted σ^2 values. The fitting range is between 1.5 and 6 Å. The k^3 weighted data are transformed between 2.5 – 13 Å^{-1}. The data have 29.8 independent data points and 12 variables were allowed to float during the fit. Au sink represents all multiple scattering pathways within the range, which were added to the fit and the same variable used for deviations in distances and disorder parameters to limit the number of variables used in the fit.
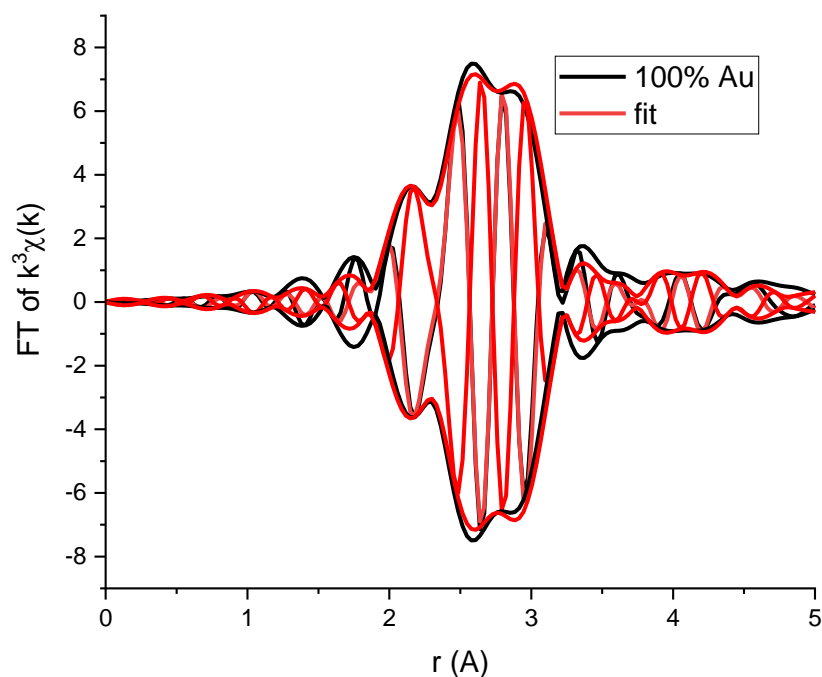
Sample	Path	N	R (Å)	σ^2 (Å^2)	ΔE_0 (eV)
100% Au NPs	Au-Au	12(1)	2.859(6)	0.0087(7)	5.3(6)
	Au-Au	5(1)	4.13(6)	0.014(8)	
	Au-Au	20(10)	4.92(9)	0.025(3)	
	Au sink	ΔR (Å) = 0.019(7)		0.01(14)	
S_0^2 = 0.85			**R-factor** = 0.026		

Figure S16.2 Fit results from the 100% Au NP sample. The fitting range is between 1.5 and 5 Å. The k^3 weighted data are transformed between 2.5 – 13 Å^{-1}. The data have 23.1 independent data points and 13 variables were allowed to float during the fit. Au sink represents all multiple scattering pathways within the range, which were added to the fit and the same variable used for deviations in distances and disorder parameters to limit the number of variables used in the fit. The Au sink amplitude was also a variable, and all multiple scattering pathway amplitudes were reduced by 20 % (amp$_{sink}$ = 0.8 ± 0.6).
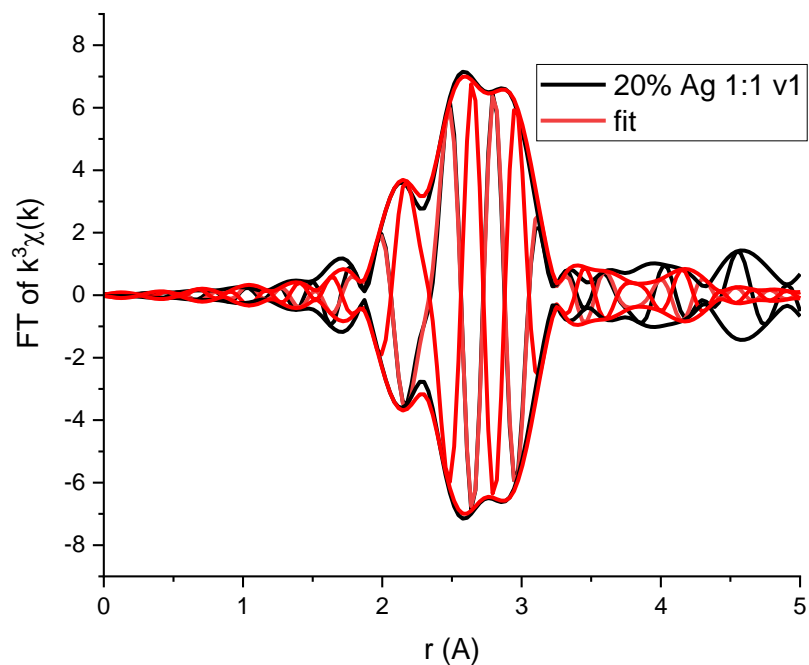
Sample	Path	N	R (Å)	σ^2 (Å^2)	ΔE_0 (eV)
20% Ag 1:1 v1 NPs	Au-Au	12(1)	2.858(4)	0.0090(6)	5.0(5)
	Au-Au	4(1)	4.04(3)	0.010(4)	
S_0^2 = 0.85			**R-factor** = 0.019		

Figure S16.3 Fit results from the 20% Ag 1:1 v1 NP sample. The fitting range is between 1.5 and 4.1 Å. The k^3 weighted data are transformed between 2.5 – 13 Å^{-1}. The data have 17.1 independent data points and 7 variables were allowed to float during the fit.
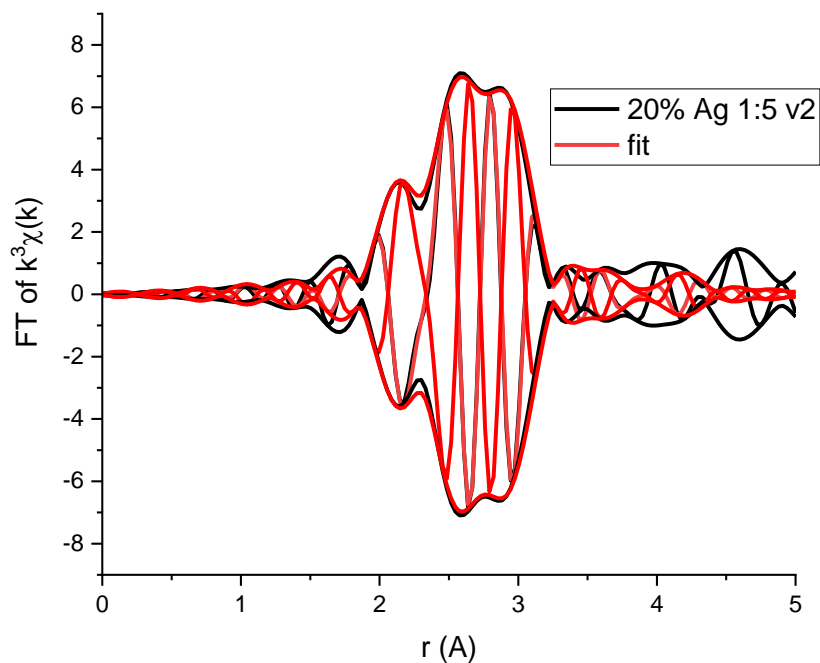
Sample	Path	N	R (Å)	σ^2 (Å^2)	ΔE_0 (eV)
20% Ag 1:5 v2 NPs	Au-Au	12(1)	2.858(4)	0.0090(6)	5.1(5)
	Au-Au	4(1)	4.03(4)	0.012(5)	
S_0^2 = 0.85			**R-factor** = 0.019		

Figure S16.4 Fit results from the 20% Ag 1:5 v2 NP sample. The fitting range is between 1.5 and 4.1 Å. The k^3 weighted data are transformed between 2.5 – 13 Å^{-1}. The data have 17.1 independent data points and 7 variables were allowed to float during the fit.
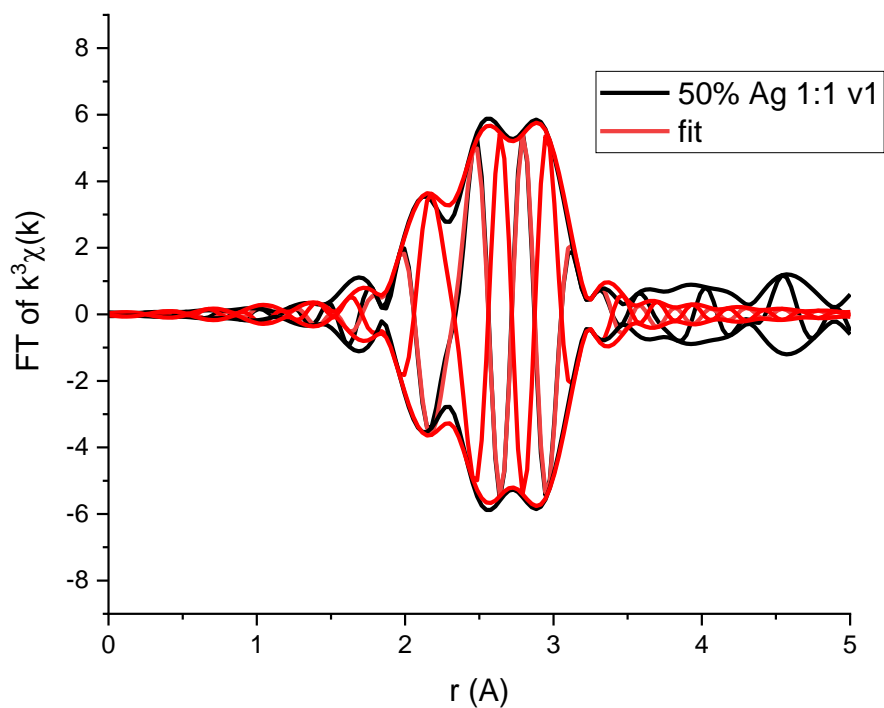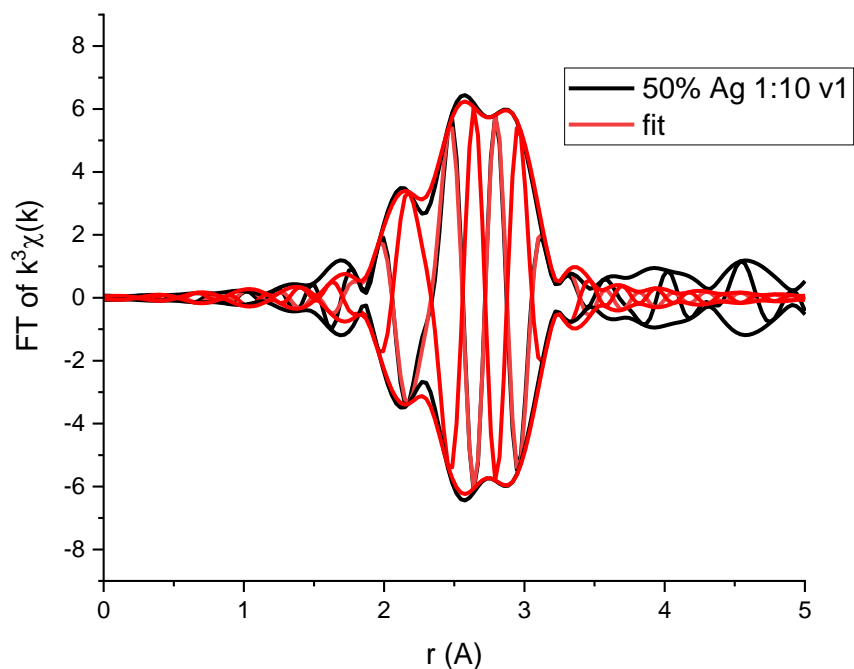
Sample	Path	N	R (Å)	σ^2 (Å²)	ΔE_0 (eV)
50% Ag 1:1 v1 NPs	Au-Au	12(1)	2.852(6)	0.0095(8)	4.3(6)
	Au-Ag	0.5(4)	2.83(6)	0.0095(8)	
S_0^2 =	0.85			R-factor = 0.011	

Figure S16.5 Fit results from the 50% Ag 1:1 v1 NP sample. The fitting range is between 1.5 and 3.5 Å. The k^3 weighted data are transformed between 2.5 – 13 Å^{-1}. The data have 13.3 independent data points and 6 variables were allowed to float during the fit.
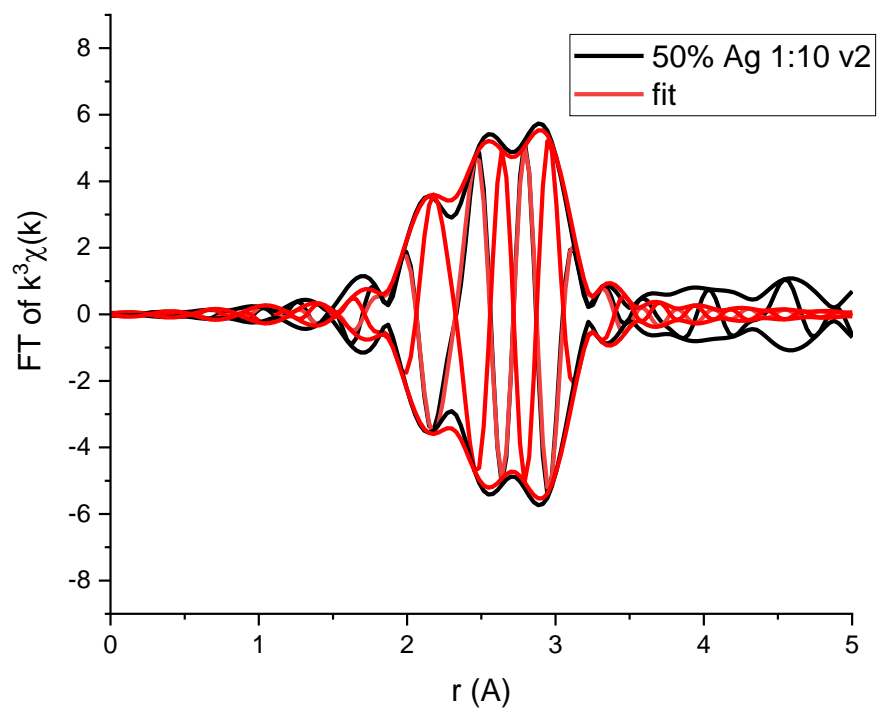
Sample	Path	N	R (Å)	σ^2 (Å^2)	ΔE_0 (eV)
50% Ag 1:10 v1 NPs	Au-Au	12.2(9)	2.852(6)	0.0099(7)	4.7(5)
	Au-Ag	0.3(6)	3.0(14)	0.0099(7)	
$S_0^2 =$ 0.85				**R-factor** = 0.010	

Figure S16.6 Fit results from the 50% Ag 1:10 v1 NP sample. The fitting range is between 1.5 and 3.5 Å. The k^3 weighted data are transformed between 2.5 – 13 Å^{-1}. The data have 13.3 independent data points and 6 variables were allowed to float during the fit.

Sample	Path	N	R (Å)	σ^2 (Å^2)	ΔE_0 (eV)
50% Ag 1:10 v2 NPs	Au-Au	11(1)	2.855(6)	0.010(1)	4.5(6)
	Au-Ag	0.9(5)	2.854(14)	0.010(1)	
$S_0^2 =$ 0.85			**R-factor** = 0.014		

Figure S16.7 Fit results from the 50% Ag 1:10 v2 NP sample. The fitting range is between 1.5 and 3.5 Å. The k^3 weighted data are transformed between 2.5 – 13 Å^{-1}. The data have 13.3 independent data points and 6 variables were allowed to float during the fit.
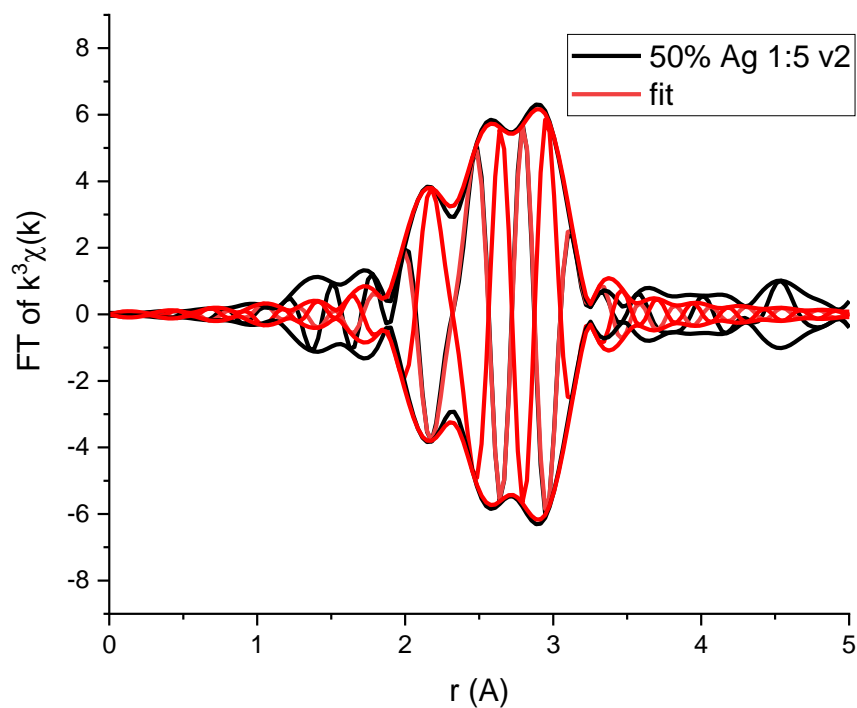
Sample	Path	N	R (Å)	σ^2 (Å²)	ΔE_0 (eV)
50% Ag 1:5 v2 NPs	Au-Au	11(1)	2.858(8)	0.010(1)	4.5(6)
	Au-Ag	0.9(5)	2.84(4)	0.010(1)	
$S_0^2 =$ 0.85			**R-factor** = 0.018		

Figure S16.8 Fit results from the 50% Ag 1:5 v2 NP sample. The fitting range is between 1.5 and 3.5 Å. The k^3 weighted data are transformed between 2.5 – 13 Å⁻¹. The data have 13.3 independent data points and 6 variables were allowed to float during the fit.
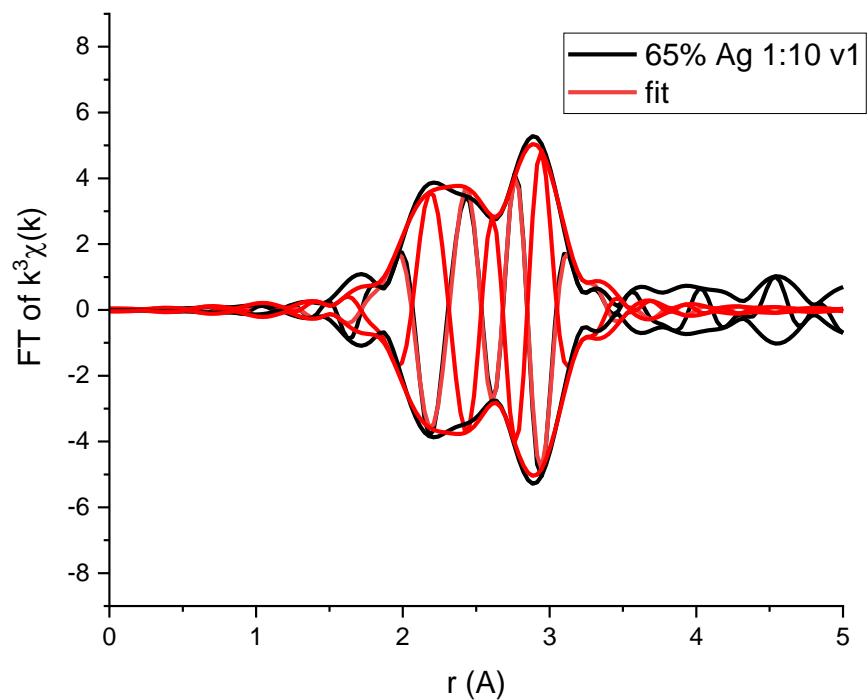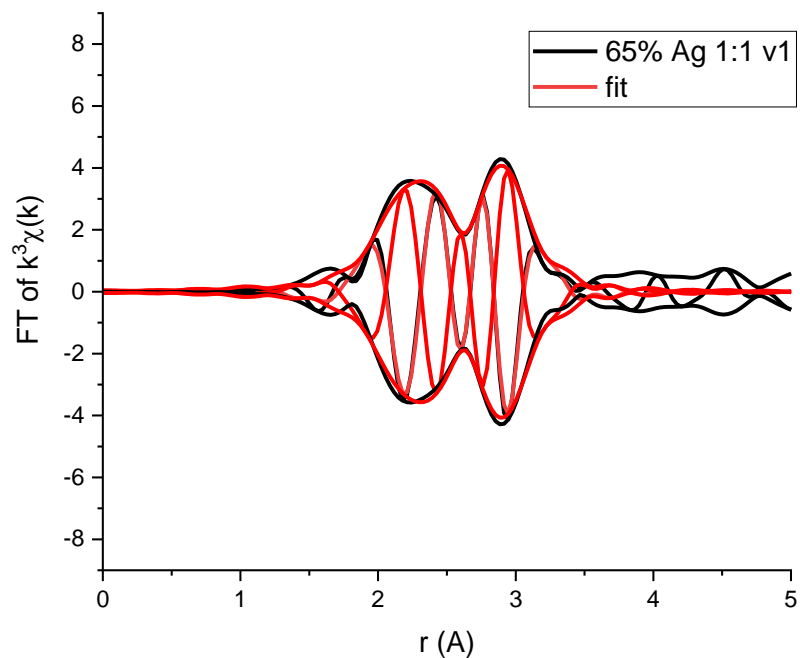
Sample	Path	N	R (Å)	σ^2 (Å²)	ΔE_0 (eV)
65% Ag 1:10 v1 NPs	Au-Au	9(1)	2.85(1)	0.010(2)	4.0(7)
	Au-Ag	3(1)	2.86(2)	0.011(3)	
$S_0^2 =$ 0.85				**R-factor** = 0.013	

Figure S16.9 Fit results from the 65% Ag 1:10 v1 NP sample. The fitting range is between 1.5 and 3.5 Å. The k^3 weighted data are transformed between 2.5 – 13 Å^{-1}. The data have 13.3 independent data points and 7 variables were allowed to float during the fit.

Sample	Path	N	R (Å)	σ^2 (Å^2)	ΔE_0 (eV)
65% Ag 1:1 v1 NPs	Au-Au	10(1)	2.85(1)	0.012(2)	4.1(6)
	Au-Ag	4(1)	2.86(2)	0.012(3)	
$S_0^2 =$ 0.85			**R-factor** = 0.0135		

Figure S16.10 Fit results from the 65% Ag 1:1 v1 NP sample. The fitting range is between 1.5 and 3.5 Å. The k^3 weighted data are transformed between 2.5 – 13 Å^{-1}. The data have 13.3 independent data points and 7 variables were allowed to float during the fit.
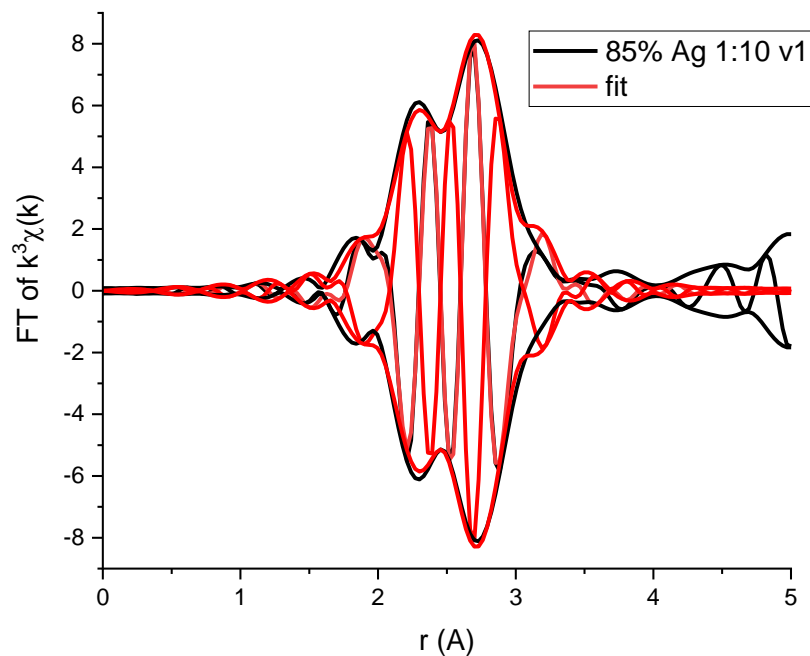
Sample	Path	N	R (Å)	σ^2 (Å^2)	ΔE_0 (eV)
85% Ag 1:10 v1 NPs	Au-Au	7(2)	2.84(2)	0.015(5)	3.3(6)
	Au-Ag	7.3(8)	2.851(8)	0.0088(9)	
S_0^2 = 0.85			**R-factor** = 0.010		

Figure S16.11 Fit results from the 85% Ag 1:10 v1 NP sample. The fitting range is between 1.5 and 3.5 Å. The k^3 weighted data are transformed between 2.5 – 13 Å^{-1}. The data have 13.3 independent data points and 7 variables were allowed to float during the fit.
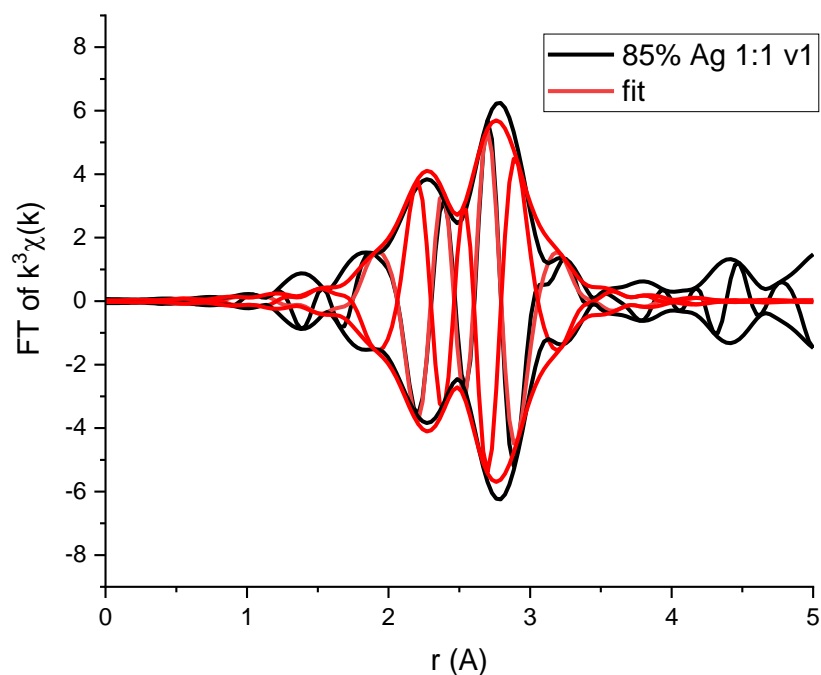
Sample	Path	N	R (Å)	σ^2 (Å^2)	ΔE_0 (eV)
85% Ag 1:1 v1 NPs	Au-Au	7(2)	2.84(2)	0.015(3)	3.5(6)
	Au-Ag	7(1)	2.857(9)	0.012(1)	
S_0^2 = 0.85				**R-factor** = 0.018	

Figure S16.12 Fit results from the 85% Ag 1:1 v1 NP sample. The fitting range is between 1.5 and 3.5 Å. The k^3 weighted data are transformed between 2.5 – 13 Å^{-1}. The data have 13.3 independent data points and 7 variables were allowed to float during the fit.
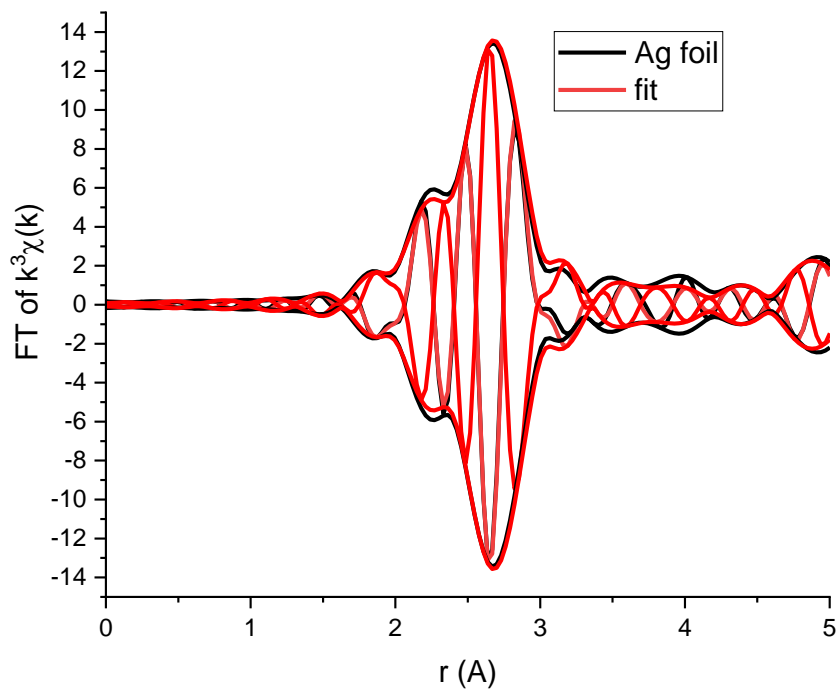
Sample	Path	*N*	*R* (Å)	σ^2 (Å^2)	ΔE_0 (eV)
Au foil (standard)	Ag-Ag	12	2.868(3)	0.0100(4)	4.1(3)
	Ag-Ag	6	4.02(2)	0.015(3)	
	Ag-Ag	24	4.99(2)	0.014(2)	
	Ag-Ag	12	4.80(3)	0.016(4)	
S_0^2 =	0.93(5)			**R-factor** = 0.019	

Figure S16.13 Fit results from bulk Ag foil. A bulk foil was fit to extract the S_0^2 parameter and to consider reasonability of NP-extracted σ^2 values. The fitting range is between 1.5 and 6 Å. The k^3 weighted data are transformed between 2.5 – 13 Å^{-1}. The data have 29.8 independent data points and 10 variables were allowed to float during the fit.
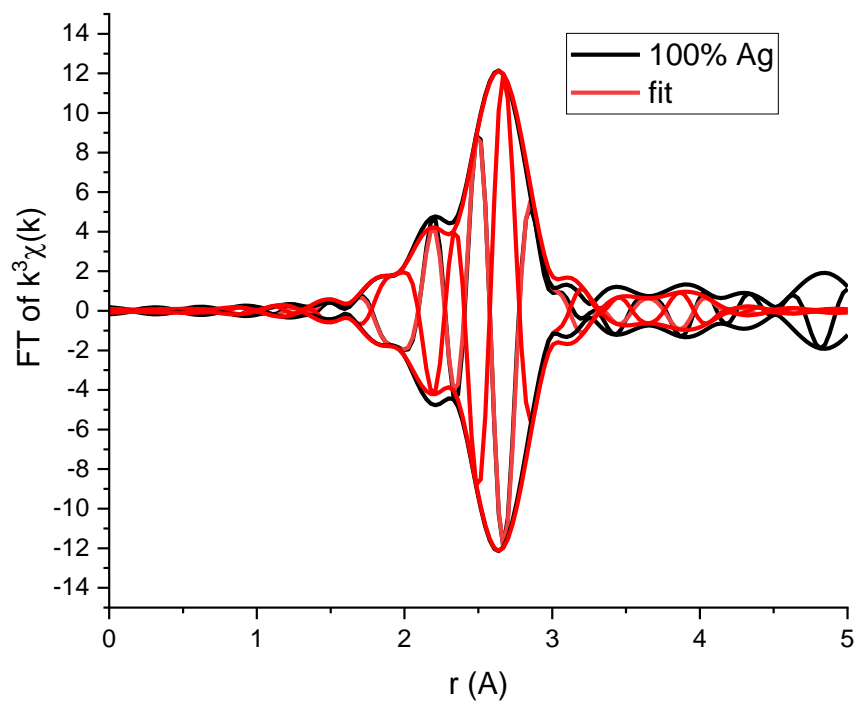
Sample	Path	N	R (Å)	σ^2 (Å²)	ΔE_0 (eV)
100% Ag NPs	Ag-Ag	12.1(8)	2.865(5)	0.0108(6)	-0.8(4)
	Ag-Ag	6(3)	4.03(3)	0.015(7)	
S_0^2 = 0.93				R-factor = 0.016	

Figure S16.14 Fit results from 100% Ag NP sample. The fitting range is between 1.5 and 4.5 Å. The k^3 weighted data are transformed between 2.5 – 13 Å^{-1}. The data have 19.8 independent data points and 7 variables were allowed to float during the fit.
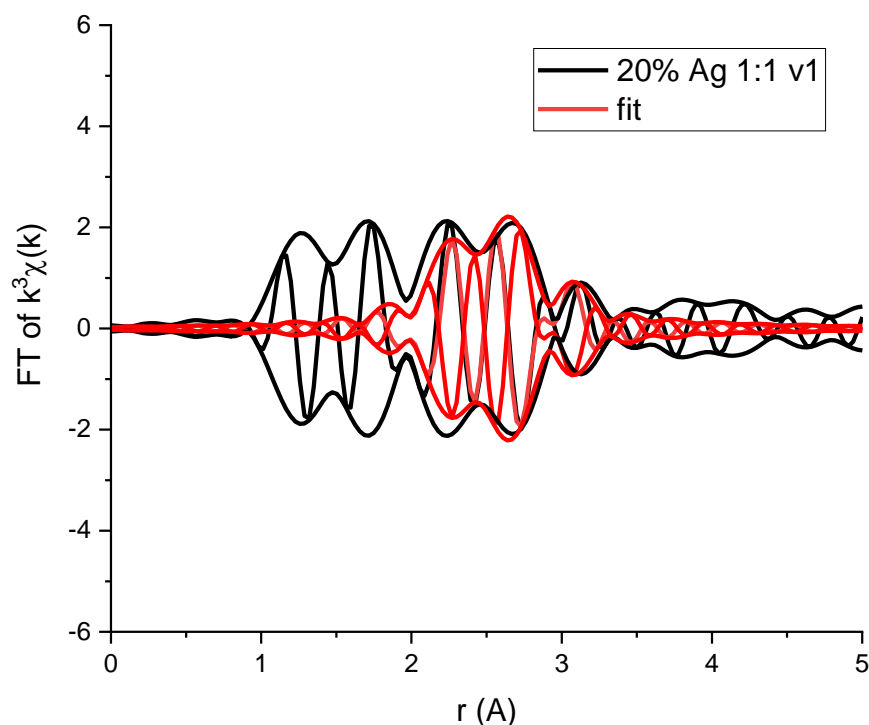
Sample	Path	N	R (Å)	σ^2 (Å^2)	ΔE_0 (eV)
20% Ag 1:1 v1 NPs	Ag-Ag	1.6(4)	2.92(2)	0.006(2)	-2(2)
	Ag-Au	1.3(4)	2.97(3)	0.006(2)	
$S_0^2 =$ 0.93			**R-factor** = 0.093		

Figure S16.15 Fit results from 20% Ag 1:1 v1 NP sample. The fitting range is between 2 and 3.5 Å. The k^3 weighted data are transformed between 2.5 – 13 Å^{-1}. The data have 9.8 independent data 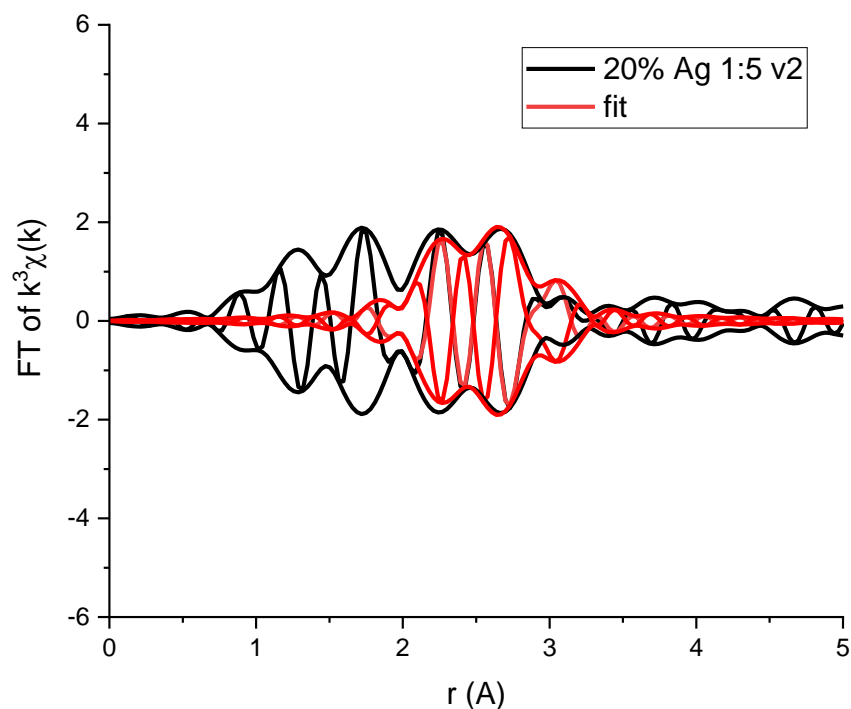points and 6 variables were allowed to float during the fit. It should be noted that despite attempts to fit the pathways below 2 Å, they could not be fit using a reasonable number of pathways, or by Ag-Cl structures alone. This suggests that the structure is complex, and that there is likely cluster formation along with the minimal incorporation observed.

Sample	Path	N	R (Å)	σ^2 (Å^2)	ΔE_0 (eV)
20% Ag 1:5 v2 NPs	Ag-Ag	1.5(3)	2.91(2)	0.006(2)	-1(1)
	Ag-Au	1.3(3)	2.95(3)	0.006(2)	
$S_0^2 =$ 0.93				**R-factor** = 0.05	

Figure S16.16 Fit results from 20% Ag 1:5 v2 NP sample. The fitting range is between 2 and 3.5 Å. The k^3 weighted data are transformed between 2.5 – 13 Å^{-1}. The data have 9.8 independent data points and 6 variables were allowed to float during the fit. It should be noted that despite attempts to fit the pathways below 2 Å, they could not be fit using a reasonable number of pathways, or by Ag-Cl structures alone. This suggests that the structure is complex, and that there is likely cluster formation along with the minimal incorporation observed.
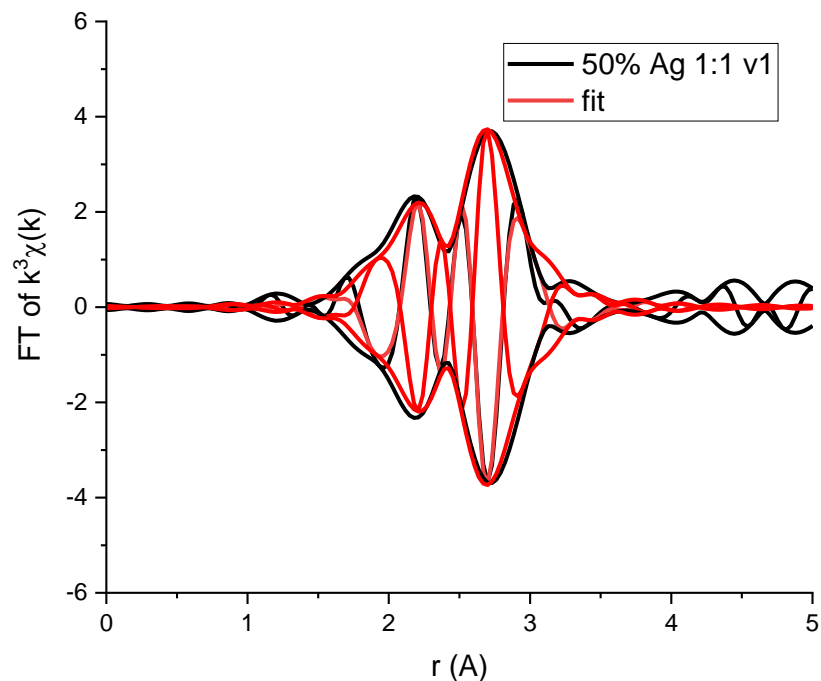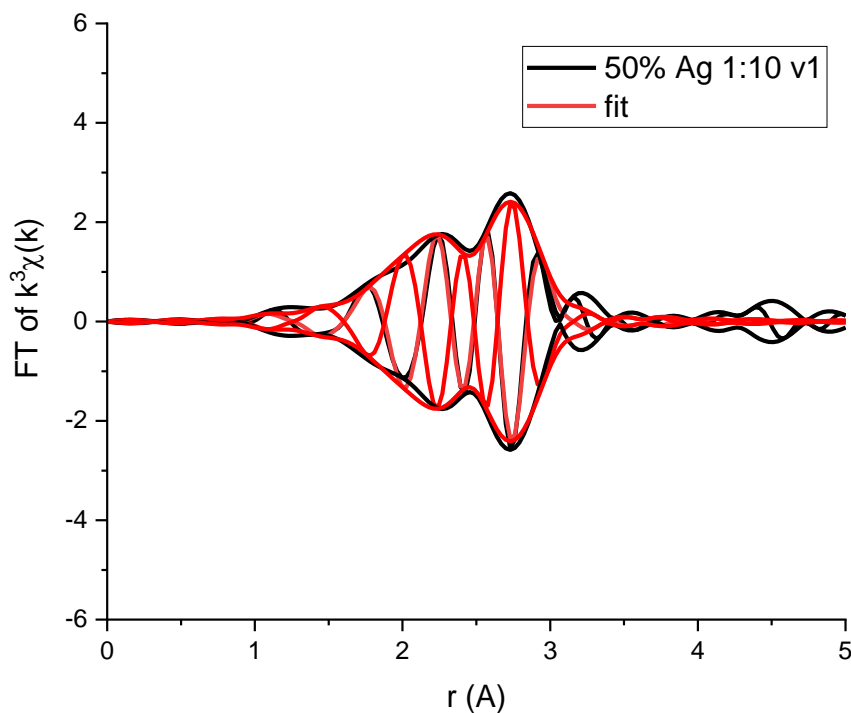
Sample	Path	N	R (Å)	σ^2 (Å^2)	ΔE_0 (eV)
50% Ag 1:1 v1 NPs	Ag-Ag	4.5(8)	2.88(1)	0.012(2)	-0.1(8)
	Ag-Au	4(2)	2.89(3)	0.017(7)	
S_0^2 = 0.93				**R-factor** = 0.024	

Figure S16.17 Fit results from 50% Ag 1:1 v1 NP sample. The fitting range is between 1.5 and 3.5 Å. The k^3 weighted data are transformed between 2.5 – 13 Å^{-1}. The data have 13.3 independent data points and 7 variables were allowed to float during the fit.

Figure S16.18 Fit results from 50% Ag 1:10 v1 NP sample. The fitting range is between 1.5 and 3.5 Å. The k^3 weighted data are transformed between 2.5 – 13 Å^{-1}. The data have 13.3 independent data points and 8 variables were allowed to float during the fit. To achieve a reasonable fit, an Ag-Cl pathway was required, suggesting a similar, but less severe trend as with the 20% samples.

Sample	Path	N	R (Å)	σ^2 (Å^2)	ΔE_0 (eV)
50% Ag 1:10 v1 NPs	Ag-Ag	0.8(6)	2.87(2)	0.015(2)	-5(1)
	Ag-Au	8(2)	2.81(2)	0.015(2)	
	Ag-Cl	2.5(9)	2.58(1)	0.014(3)	
S_0^2 = 0.93				**R-factor** = 0.028	
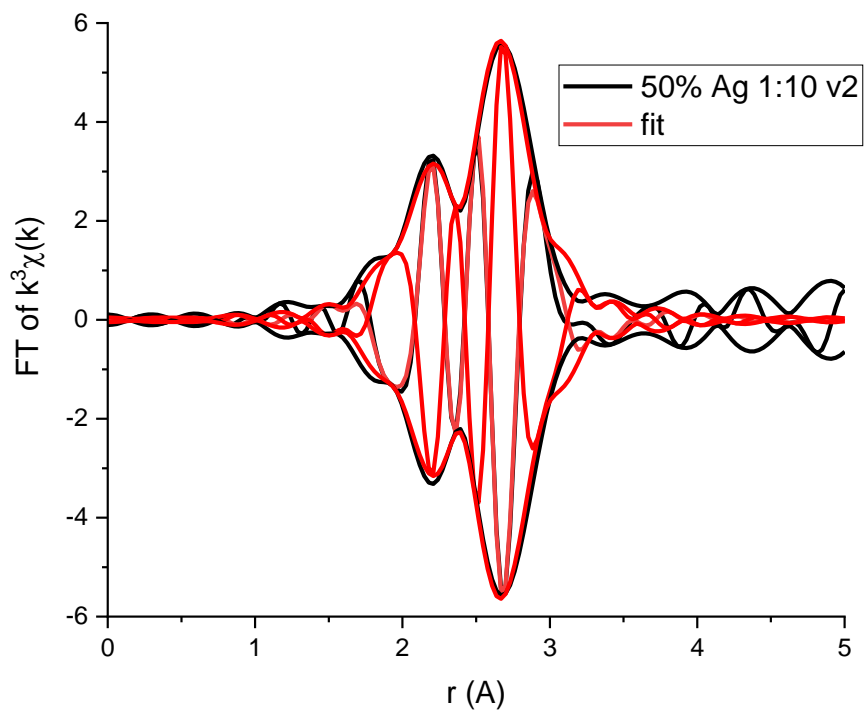
Sample	Path	N	R (Å)	σ^2 (Å^2)	ΔE_0 (eV)
50% Ag 1:10 v2 NPs	Ag-Ag	5.9(7)	2.868(9)	0.010(1)	-0.3(6)
	Ag-Au	4(1)	2.88(2)	0.013(5)	
$S_0^2 =$ 0.93				**R-factor** = 0.013	

Figure S16.19 Fit results from 50% Ag 1:10 v2 NP sample. The fitting range is between 1.5 and 3.5 Å. The k^3 weighted data are transformed between 2.5 – 13 Å^{-1}. The data have 13.3 independent data points and 7 variables were allowed to float during the fit.
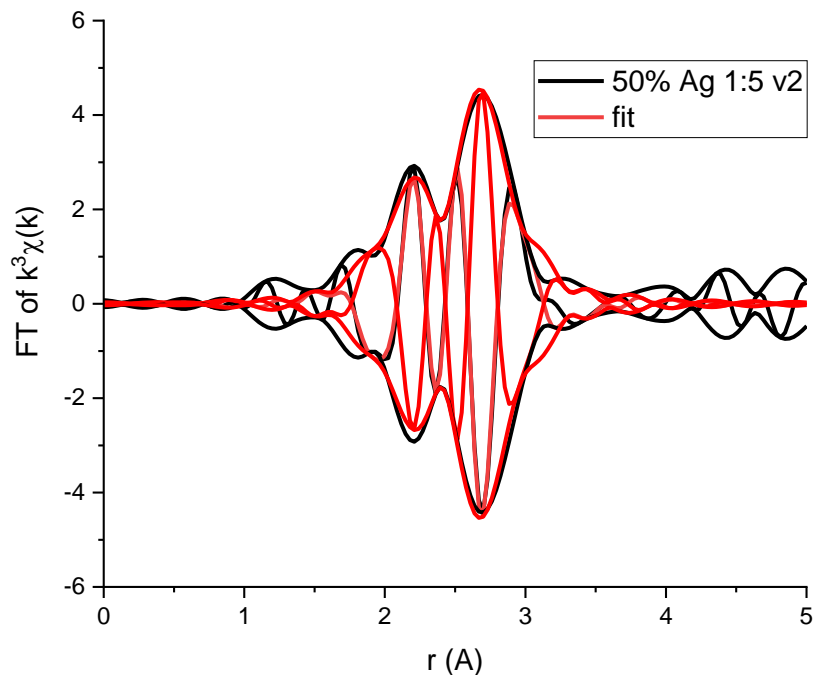
Sample	Path	N	R (Å)	σ^2 (Å^2)	ΔE_0 (eV)
50% Ag 1:5 v2 NPs	Ag-Ag	4.9(7)	2.88(1)	0.011(1)	-0.3(7)
	Ag-Au	4(1)	2.89(2)	0.015(5)	
S_0^2 = 0.93				**R-factor** = 0.018	

Figure S16.20 Fit results from 50% Ag 1:5 v2 NP sample. The fitting range is between 1.5 and 3.5 Å. The k^3 weighted data are transformed between 2.5 – 13 Å^{-1}. The data have 13.3 independent data points and 7 variables were allowed to float during the fit.
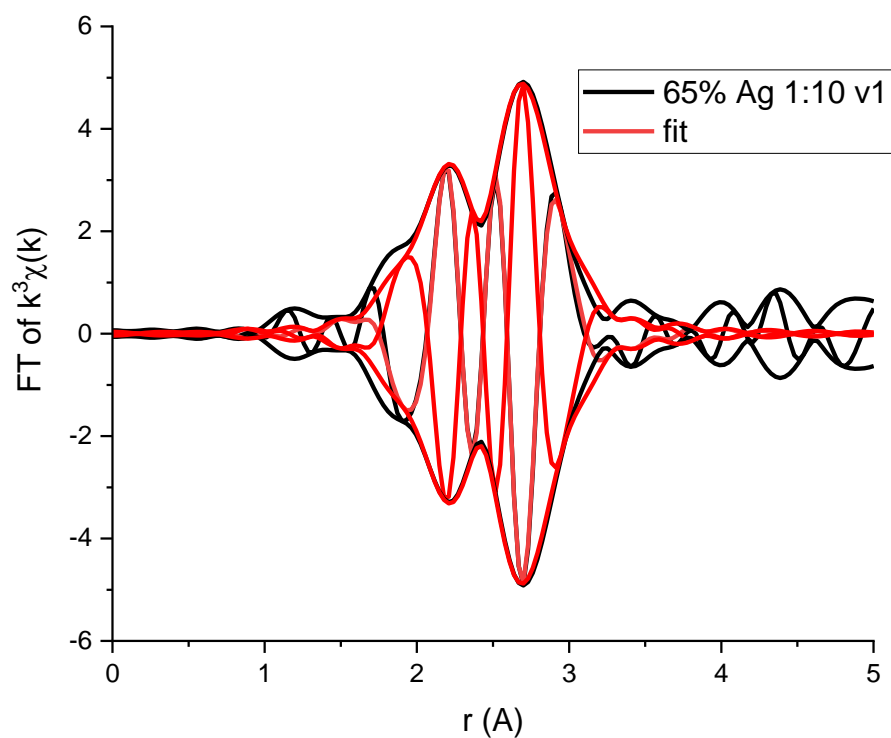
Sample	Path	N	R (Å)	σ^2 (Å^2)	ΔE_0 (eV)
65% Ag 1:10 v1 NPs	Ag-Ag	4.9(6)	2.86(1)	0.013(3)	-0.8(6)
	Ag-Au	6(1)	2.86(2)	0.010(1)	
S_0^2 = 0.93				**R-factor** = 0.013	

Figure S16.21 Fit results from 65% Ag 1:10 v1 NP sample. The fitting range is between 1.5 and 3.5 Å. The k^3 weighted data are transformed between 2.5 – 13 Å^{-1}. The data have 13.3 independent data points and 7 variables were allowed to float during the fit.
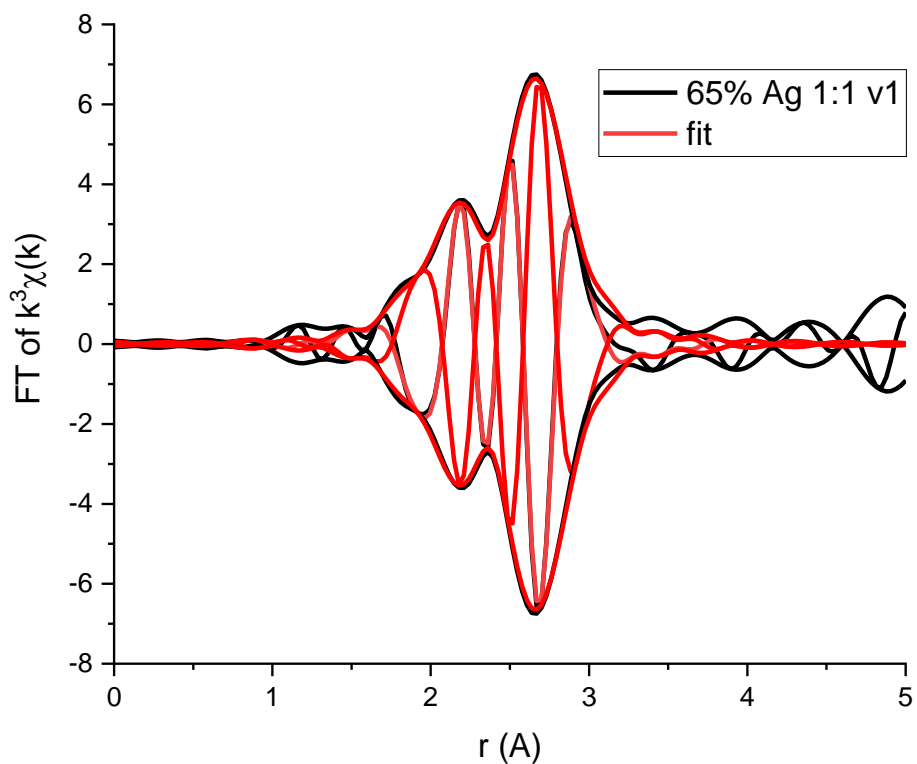
Sample	Path	N	R (Å)	σ^2 (Å²)	ΔE_0 (eV)
65% Ag 1:1 v1 NPs	Ag-Ag	7.1(7)	2.856(7)	0.011(1)	-1.6(5)
	Ag-Au	3.9(6)	2.85(2)	0.011(1)	
S_0^2 = 0.93			**R-factor** = 0.007		

Figure S16.22 Fit results from 65% Ag 1:1 v1 NP sample. The fitting range is between 1.5 and 3.5 Å. The k^3 weighted data are transformed between 2.5 – 13 Å^{-1}. The data have 13.3 independent data points and 6 variables were allowed to float during the fit.
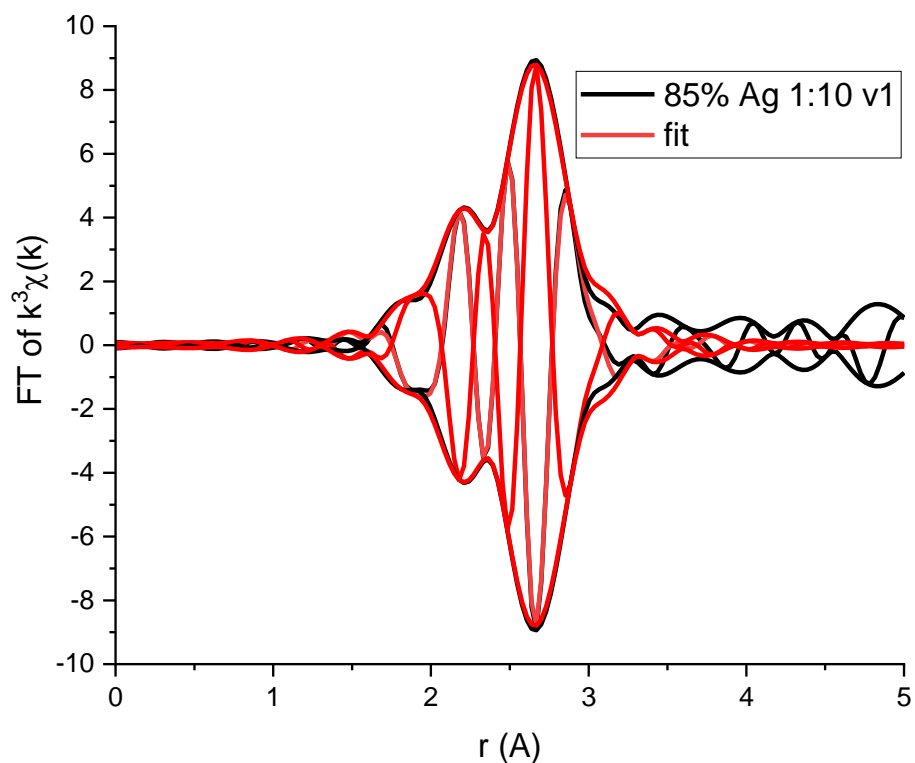
Sample	Path	N	R (Å)	σ^2 (Å²)	ΔE_0 (eV)
85% Ag 1:10 v1 NPs	Ag-Ag	8.6(7)	2.858(6)	0.0102(8)	-0.8(4)
	Ag-Au	2.7(6)	2.87(2)	0.0102(8)	
S_0^2 =	0.93			**R-factor** = 0.005	

Figure S16.23 Fit results from 85% Ag 1:10 v1 NP sample. The fitting range is between 1.5 and 3.5 Å. The k^3 weighted data are transformed between 2.5 – 13 Å^{-1}. The data have 13.3 independent data points and 6 variables were allowed to float during the fit.
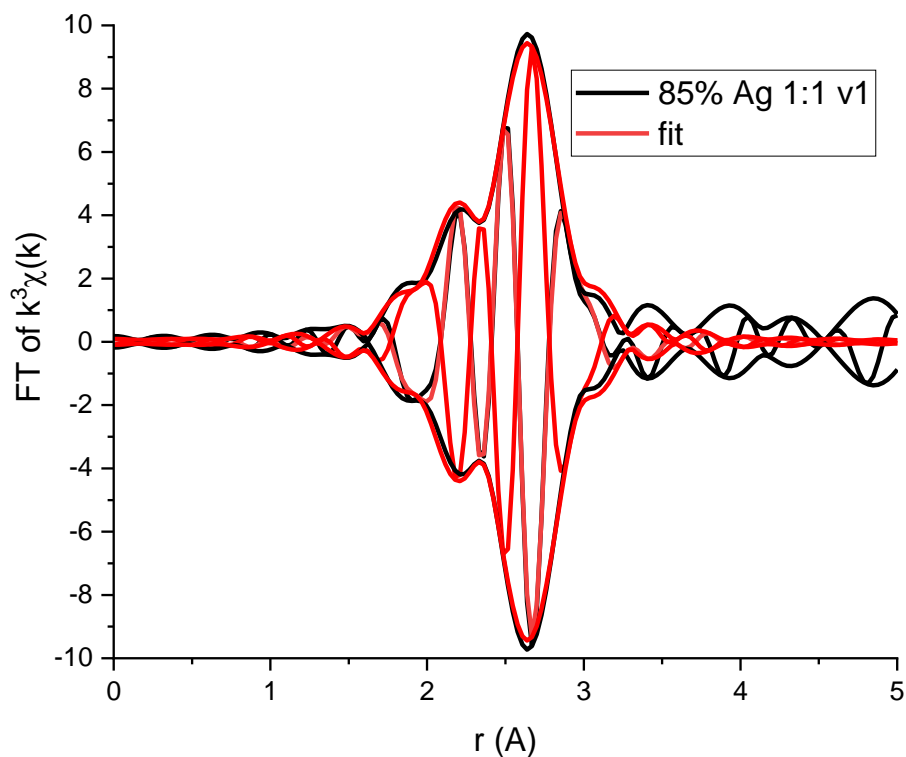
Sample	Path	N	R (Å)	σ^2 (Å^2)	ΔE_0 (eV)
85% Ag 1:1 v1 NPs	Ag-Ag	8.9(7)	2.861(6)	0.0099(7)	-0.7(5)
	Ag-Au	2.4(7)	2.88(3)	0.0099(7)	
S_0^2 = 0.93				**R-factor** = 0.007	

Figure S16.24 Fit results from 85% Ag 1:1 v1 NP sample. The fitting range is between 1.5 and 3.5 Å. The k^3 weighted data are transformed between 2.5 – 13 Å^{-1}. The data have 13.3 independent data points and 6 variables were allowed to float during the fit.

Calculation of Cowley's parameter

Cowley's parameter[11] as reported in Table 1 of the manuscript was calculated as has previously been reported for alloy NPs[12] according to Eq. S1, where N_{AB} is the coordination number associated with multimetallic (A-B) bonding, N_{AM} is the total coordination number and x_B is the fraction of metal B in the NPs.

$$\alpha = 1 - \frac{N_{AB}/N_{AM}}{x_B} \tag{S2}$$

Ag and Au domain size estimation within AgAu NPs

The size of Ag and Au domains in the AgAu nanoparticles were estimated using the method reported by Calvin et. al,[13] which uses XAFS-derived coordination numbers to determine particle size (Eq. S2), where N_{nano} is the XAFS-derived coordination number for Au-Au or Ag-Ag within the particles, $N_{bulk} = 12$ (for FCC Ag or Au), r is the nearest-neighbor distance (2.884 Å) and R is the radius of the Au or Ag cluster size.

$$N_{nano} = [1 - \frac{3}{4}\left(\frac{r}{R}\right) + \frac{1}{16}\left(\frac{r}{R}\right)^3]N_{bulk} \tag{S3}$$

Results from this analysis are shown in the table below:

Table S8. Domain size estimates for local Au and Ag clustering

sample	Au cluster radius	Ag cluster radius
100% Au	9.7 nm	N/A
20% Ag 1:1 v1	fully coordinated	0.21 nm
20% Ag 1:5 v2	fully coordinated	0.21 nm
50% Ag 1:1 v1	8.1 nm	0.32 nm
50% Ag 1:10 v1	fully coordinated	0.19 nm
50% Ag 1:10 v2	4.3 nm	0.41 nm
50% Ag 1:5 v2	2.0 nm	0.35 nm
65% Ag 1:10 v1	1.0 nm	0.34 nm
65% Ag 1:1 v1	1.2 nm	0.51 nm
85% Ag 1:10 v1	0.5 nm	0.76 nm
85% Ag 1:1 v1	0.5 nm	0.83 nm
100% Ag	N/A	fully coordinated

Determination of fraction of Ag in AgAu NPs that is on the NP surface

Coordination numbers (CNs) extracted from EXAFS analysis were used to determine the fraction (x_{Ag}) of Ag atoms in the AgAu NPs that reside on the NP surface. $CN_{Ag} = 12$ would indicate all Ag are in the bulk of the NP, i.e. $x_{Ag} = 0$. Whereas $CN_{Ag} < 12$ indicates that $x_{Ag} > 0$, meaning that some fraction of the incorporated Ag is on the NP surface. If we assume that the surfaces of the NPs consist of primarily {111} facets, which is likely due to this being the lowest energy, then an atom within a surface layer will have $CN_{Ag} = 9$, and it follows that:

$$x_{Ag} = \frac{12 - CN_{Ag}}{3} \qquad\qquad (S4)$$

The results for each sample are shown in Table SX and compared with the overall fraction of surface atoms in the NP, which was calculated using geometry and the NP size dimensions derived from SAXS analysis.

Table S9. Fraction of Ag on the NP surface vs. interior compared with total fraction of atoms on NP surface

sample	X_{Ag} on surface	X_{atoms} on surface
100% Au	0	0.1
20% Ag 1:1 v1	3 ± 0.6	0.08
20% Ag 1:5 v2	3.1± 0.5	0.099
50% Ag 1:1 v1	1.1 ± 0.2	0.097
50% Ag 1:10 v1	1.0 ± 0.3	0.090
50% Ag 1:10 v2	0.8 ± 0.1	0.104
50% Ag 1:5 v2	1.0 ± 0.2	0.089
65% Ag 1:10 v1	0.48 ± 0.06	0.106
65% Ag 1:1 v1	0.32 ± 0.03	0.070
85% Ag 1:10 v1	0.24 ± 0.02	0.088
85% Ag 1:1 v1	0.23 ± 0.02	0.074
100% Ag	-0.0037 ± 0.002	0.028

Note that the unphysical values for the 20% samples above result due to the severely undercoordinated Ag, which as discussed in the manuscript, suggests that the Ag in these samples is in majority not incorporated into the NPs.

References

1. J. Ilavsky, *Journal of Applied Crystallography*, 2012, **45**, 324-328.
2. J. Ilavsky and P. R. Jemian, *Journal of Applied Crystallography*, 2009, **42**, 347-353.
3. B. Ravel, M. Newville, J. O. Cross and C. E. Bouldin, *Physica B*, 1995, **208 & 209**, 145-147.
4. Y. Yang, W. Liu, X. Gao and M. Chen, *Hydrometallurgy*, 2019, **186**, 252-259.
5. B. Ravel and M. Newville, *J. Synchrotron Radiat.*, 2005, **12**, 537-541.
6. B. Ravel, *J. Synchrotron Radiat.*, 2001, **8**, 314-316.
7. E. A. Stern, *Contemp. Phys.*, 1978, **19**, 289-310.
8. E. A. Stern, *Phys. Rev. B*, 1974, **10**, 3027-3037.
9. B. Ravel and S. D. Kelly, *AIP Conf. Proc.*, 2007, **882**, 150-152.
10. R. Scott, *Physical Methods in Bioinorganic Chemistry: Spectroscopy and Magnetism*, University Science Books, 2000.
11. J. M. Cowley, *Physical Review*, 1965, **138**, A1384-A1389.
12. A. I. Frenkel, A. Yevick, C. Cooper and R. Vasic, *Annual Review of Analytical Chemistry*, 2011, **4**, 23-39.
13. S. Calvin, M. M. Miller, R. Goswami, S. F. Cheng, S. P. Mulvaney, L. J. Whitman and V. G. Harris, *Journal of Applied Physics*, 2003, **94**, 778-783.